Materials Horizons

ROYAL SOCIETY OF CHEMISTRY

REVIEW

View Article Online
View Journal | View Issue



Cite this: *Mater. Horiz.*, 2025, 12, 2878

# Multifunctional solar-driven interfacial evaporation system for simultaneous clean water production and high-value-added ion extraction

Jing Wu,†[a] Guang Yin,†[b] Ji Liu,*[ac] Zhong-Zhen Yu *[b] and Xiaofeng Li *[a]

Received 18th December 2024,
Accepted 10th February 2025

DOI: 10.1039/d4mh01857e

rsc.li/materials-horizons

The utilization of solar-driven interfacial evaporation (SIE) technology for clean water production has rapidly expanded, driven by global clean water scarcity and the energy crisis. Recent developments have demonstrated that combining SIE technology with the ion extraction process enables the effective use of abundant sunlight to economically and sustainably harvest high-value minerals from the ocean while simultaneously producing clean water. This synergy not only maximizes resource recovery but also enhances the ecological and economic benefits of solar energy utilization. In this review, we provide a comprehensive overview of the materials and methodologies used in designing multifunctional SIE systems for simultaneous clean water production and high-value ion extraction. The design rationale behind these multifunctional SIE systems, along with various ion extraction strategies and mechanisms, has been thoroughly discussed, identifying both the prevailing challenges and the potential research opportunities in this evolving field. This review aims to highlight the significant potential of SIE technology not only in enhancing clean water availability but also in contributing to sustainable energy and resource management.



**Wider impact**

We believe that this review will inspire readers' interest in high-value-added ion extraction during the solar-driven interfacial evaporation (SIE) process. Driven by global freshwater scarcity and the energy crisis, SIE technology has emerged as a green and sustainable solution for clean water production. Recent advancements have also shown that integrating SIE technology with ion extraction processes enables the development of multifunctional SIE systems. These systems more efficiently utilize abundant solar energy to harvest high-value minerals economically and sustainably from the ocean and wastewater while simultaneously producing freshwater. This review aims to highlight the significant potential of SIE technology not only in enhancing freshwater availability and contributing to sustainable energy and resource management. We have provided a comprehensive and accessible overview of the materials and methodologies for designing multifunctional SIE systems for simultaneous freshwater production and high-value ion extraction. The design rationale behind these multifunctional SIE systems, along with various ion extraction strategies and mechanisms, has also been thoroughly discussed, identifying both the prevailing challenges and the potential research opportunities in this evolving direction. We believe that in-depth researches in this direction could catalyze a new wave of innovation in the field of solar-powered water treatment.

## 1. Introduction

Water scarcity has emerged as a global challenge due to uneven distribution, contamination, drought and other pressing issues.[1] Currently, over 1.6 billion people reside in water-stressed areas without access to clean and safe drinking water and this situation is expected to intensify further in the coming decades.[2] Existing technologies for clean water production such as multistage flash distillation, multi-effect distillation, vapor compression, reverse osmosis and electrodialysis address water scarcity but highly rely on fossil energy, exacerbating environmental challenges.[3] Solar energy, as an inexhaustible renewable resource, emerges as a promising alternative to traditional fossil fuels, playing a crucial role in promoting sustainable development. Leveraging this naturally abundant and green solar energy, innovative technologies like solar-driven interfacial evaporation (SIE) have been developed to offer viable and sustainable solutions for producing clean water, effectively addressing the global issue of

[a] State Key Laboratory of Organic–Inorganic Composites, College of Materials Science and Engineering, Beijing University of Chemical Technology, Beijing 100029, China. E-mail: jliu@mail.buct.edu.cn, xfli@mail.buct.edu.cn
[b] Beijing Key Laboratory of Advanced Functional Polymer Composites, Beijing University of Chemical Technology, Beijing 100029, China. E-mail: yuzz@mail.buct.edu.cn
[c] School of Chemistry, Trinity College Dublin, D2, Dublin, Ireland
† The authors contributed equally to this work.

clean water scarcity in an environmentally sustainable manner.[4–6] In the past few years, researches have primarily focused on enhancing the energy efficiency and evaporation performance of single-function solar evaporators and ultrahigh clean water production rates have been successfully achieved. However, the potential for acquiring and collecting high-value ions from seawater and wastewater has often been overlooked in this field.

Beyond sodium chloride (NaCl), the most abundant salt in oceans, there are also significant amounts of essential metal elements such as lithium and uranium in seawater and brines.[7] Lithium, critical for renewable energy storage systems,[8–11] is extensively utilized in high-energy rechargeable batteries, aerospace and nuclear power generation.[12,13] However, the price of lithium remains quite high, which has also surged dramatically, increasing tenfold from $6000 per ton in 2016 to nearly $60 000 per ton in 2022.[14] This trend of rising prices and fluctuations is anticipated to persist due to the rapid advancement and widespread adoption of new energy technologies, such as trams and various electronic devices. With global conventional lithium reserves projected to be depleted by 2080, there is increasing interest in exploiting unconventional lithium sources. The estimated reserve of lithium in seawater is approximately 230 million tons, which is about 5000 times more than the nearly 14 million tons of lithium found in land-based resources.[15] Similarly, uranium, crucial for green and reliable nuclear energy, is also predominantly found in the oceans. Approximately 99.8% of the uranium of the world with a total content of 4.5 billion tons is located in the oceans, making it 1000 times more abundant than the amount found in terrestrial uranium mines.[16–19] Therefore, extracting lithium and uranium from seawater not only offers a sustainable solution to the scarcity of these critical resources but also reduces the environmental impact associated with traditional mining processes.[20]

Recent developments have shown that integrating SIE technology with the ion extraction process allows industries to effectively utilize abundant sunlight to economically and sustainably harvest high-value minerals from the ocean while producing clean water.[21–26] The SIE typically includes key processes such as solar-thermal conversion, liquid transport and solute diffusion. These processes lead to an increase in temperature and the formation of localized high-concentration fields, thus accelerating the ion adsorption kinetics and facilitating the extraction without requiring additional energy input.[27,28] In addition, the adsorbents for ion extraction are usually powders. When these powders are immobilized in solar evaporators, their formability, durability and recyclability can be significantly improved. Moreover, the capillary effect and rapid water transport capability of the structurally engineered solar evaporators help replenish, diffuse and enrich ions, mitigating issues caused by the accumulation of interfering ions that can obstruct the enrichment of target ions due to concentration polarization.[29] Therefore, the design of multifunctional SIE systems represents a viable yet promising solution in addressing the long-standing environmental and resource scarcity issues, offering an opportunity to start a revolution in the field of clean water production and marine chemical industry.

Although great progress has been achieved, there is still a lack of comprehensive summaries and guidances on the fabrication of multifunctional SIE systems for simultaneous clean water production and high-value ion extraction, nor an in-depth discussion of the advancements in this field. To this end, this review aims to provide a comprehensive and accessible overview, focusing on the management strategies of optimized SIE process for simultaneous desalination and mineral ion extraction, including traditional NaCl collection and other high-value trace ions extraction. A range of stimulating examples is presented, emphasizing zero liquid discharge (ZLD) strategies through specific-site crystallization, lubricated surface construction and component separation, as well as efficient mineral ion extraction techniques that leverage the adsorption process, differences in ion mobility and membrane separation (Fig. 1). The fundamental principles behind these strategies and techniques are also thoroughly discussed, compared and analyzed. Finally, current challenges and future research opportunities are proposed.

## 2. Mechanisms for SIE and ion extraction

### 2.1 Basis of solar-thermal conversion

The solar-thermal conversion and utilization capabilities of an SIE system are crucial for enhancing the evaporation rate and improving ion extraction efficiency. Key elements in the solar-thermal conversion process include solar absorbance, conversion mechanism and heat management, all of which can be optimized through strategic material selection and structural engineering. When the surface of a solar-thermal material is exposed to solar radiation, some of the photon energy can be converted into heat.[30–34] Solar absorbance refers to the ratio of total solar radiation absorbed by a solar-thermal material to the total incident solar radiation. To achieve efficient solar absorption, materials should absorb as much solar radiation as possible across the wavelength range of 200 nm to 2500 nm while minimizing reflectance.[35,36] Depending on the type of the solar-thermal materials, common solar-thermal conversion mechanisms include localized surface plasmon resonance (LSPR) effect, non-radiative relaxation and molecular thermal vibration.[37]

**2.1.1 LSPR effect.** This effect commonly emerges in metal nanomaterials that contain free electrons and can function similarly to a plasma system.[38] When exposed to external solar irradiation, the free electrons in the outer layers of metal nanoparticles can move, generating a new electric field. This electric field exerts a linear restoring force within the metal nanoparticles, inducing electronic dipole oscillations known as the LSPR effect.[39,40] This phenomenon leads to strong light absorption and initiates the plasmon-assisted solar-thermal effect (Fig. 2a). The efficiency of the LSPR effect is significantly influenced by factors such as shape, size, dielectric coating,

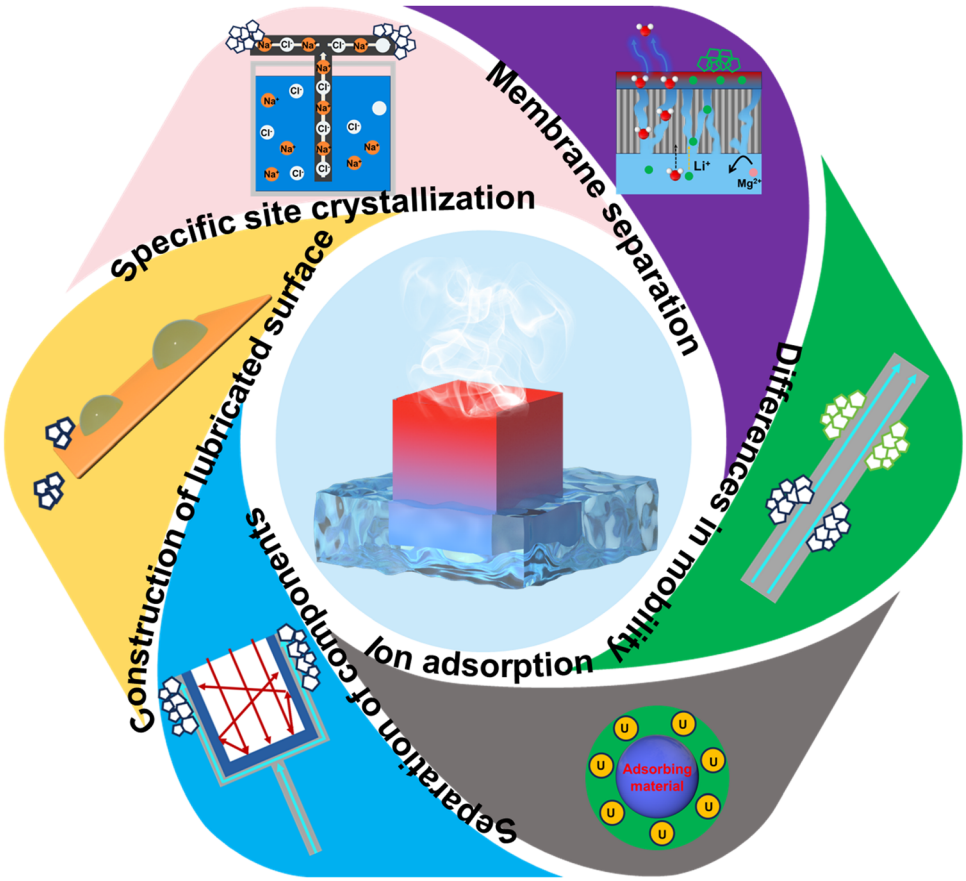


Fig. 1 Schematic illustrating the strategies for developing multifunctional SIE systems capable of extracting high-value ions.

surrounding medium and the assembly state of the metallic nanostructure.[41,42] Some metal-based plasmonic nanoparticles such as copper, titanium and barium, however, are generally limited in their efficiency for solar-thermal conversion as they typically absorb light at only one or a few specific wavelengths.[43,44] Currently, gold and silver are the predominant materials used for inducing the LSPR effect in solar-thermal applications due to their significant advantages, such as strong plasmonic resonance and minimal plasmonic losses in the visible to near-infrared spectrum and high chemical stabilities.[45–47] To improve the LSPR effect, strategies such as reducing the shape symmetries and creating hollow structures have also been proposed, which are demonstrated to be effective in broadening the LSPR spectral band. In addition, reducing the size of the metal particles or altering the surrounding medium can lead to a shift of the LSPR spectral band, accompanied by some degree of auxiliary broadening of the absorption spectrum.[48]

**2.1.2 Non-radiative relaxation.** Non-radiative relaxation is a common phenomenon in semiconductor materials, where the optical absorption spectra depend on the band gap energy. When semiconductor materials are exposed to light, electrons can be excited from the valence band (VB) to the conduction band (CB), creating holes in the VB and free electrons in the CB. These electrons and holes then return to their lower-energy states, releasing energy either through non-radiative relaxation *via* phonons or through radiative relaxation in the form of photons.[49] The process of diffusion and recombination of photoexcited carriers can lead to increases in temperature, ensuring a solar-thermal effect (Fig. 2b).[50,51] The efficiency of light-to-heat conversion in semiconductors can be enhanced through methods such as doping or the introduction of vacancies, which can alter the band energy or introduce new energy states within the bandgap, thus optimizing the thermal response under illumination.[30]

**2.1.3 Molecular thermal vibration.** Organic materials, particularly those with carbon elements or conjugated structures, are effective in absorbing solar energy, which leads to lattice vibrations that generate heat through transitions in the π bonds. Typically, conjugated π bonds can induce a red shift in the absorption spectrum. As the number of π bonds increases, the energy gap between the highest occupied molecular orbital (HOMO) and the lowest unoccupied molecular orbital (LUMO) narrows, allowing electrons to be excited by nearly any wavelength of solar light, a process associated with various π–π* transitions. This characteristic causes organic materials to appear black and exhibit excellent light-absorbing properties (Fig. 2c).[52] During the solar-thermal process, heat is generated when photo-excited electrons relax through scattering in the form of electron–electron or electron–phonon interactions, resulting in an overall temperature increase.

 

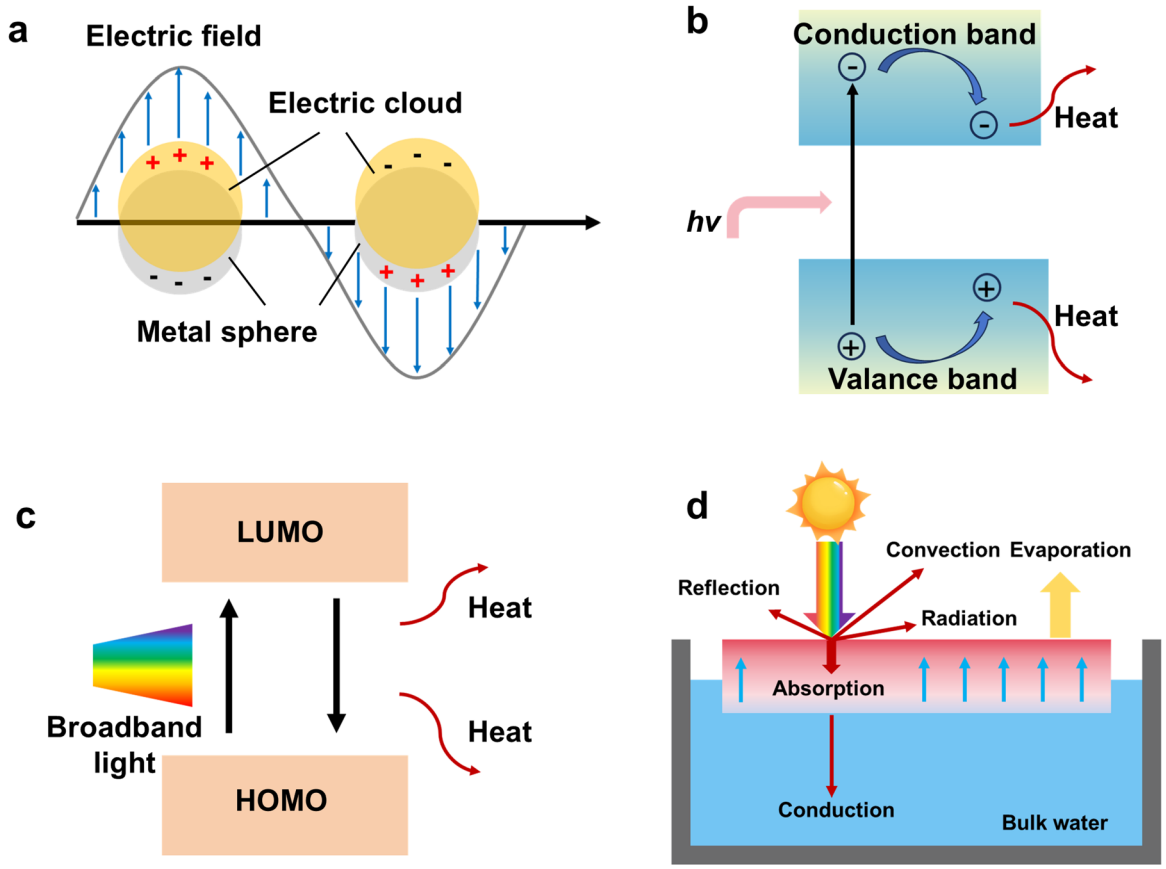


Fig. 2 Mechanisms of the solar-thermal effect: (a) Localized surface plasmon resonance effect. (b) Nonradiative relaxation. (c) Molecular thermal vibration. (d) Schematic diagram of solar-thermal conversion.

After the solar-thermal process, the generated energy can be released in several ways, including direct temperature rise in the solar-thermal material, heat radiation loss at the interface between the solar-thermal material and the surrounding air and heat convection and heat conduction losses during the heat transfer process (Fig. 2d). To enhance the efficiency of SIE, strategies should be proposed involving the careful selection of solar-thermal materials and optimized structural design to maximize the fraction of energy directed toward the evaporation process while minimizing energy loss in other forms.

### 2.2 Ions extraction mechanisms

To extract high-value ions (*e.g.*, sodium ion, $Na^+$) from water, the ZLD method is commonly utilized. It allows salt crystals to form and accumulate on the surface of the SIE device, facilitating their collection. Besides, using chemical adsorbents with a mass transfer mechanism is particularly prevalent and promising.[53] This process transfers substances from the liquid phase to the surface of a solid phase, where ions can adhere through physicochemical interactions. Adsorbent materials are pivotal in the adsorption process, affecting both the adsorption capacity and efficiency. The mechanisms of adsorption also vary based on the type of material used. For instance, some inorganic materials like $Li_4Ti_5O_{12}$ (LTO) function as $Li^+$ sieves for its recovery, showing an ion-exchange mechanism.[54] The tetrahedral 8a sites within the spinel structure of LTO can be occupied by $Li^+$, suitable for $Li^+$ insertion and extraction under both alkaline and acidic conditions (Fig. 3a). Organic materials like metal–organic frameworks (MOFs), which consist of metal ions or clusters coordinated with organic ligands, are also effective for ion separation applications because of their angstrom-sized porous structures and adjustable host–guest interactions between the frameworks and the ions.[20] The geometry and pore size of MOFs, which are determined by their crystal structures, can be precisely controlled by selecting different ligands (Fig. 3b).[55] Meanwhile, the interaction between MOFs and ions, as well as their ion selectivity, can be adjusted by modifying the type of charge and charge density within the framework. This customization has been achieved by adding functional groups, either by attaching them directly to the ligands or by filling the framework cavities with functional molecules or polymers (Fig. 3c and d).[56,57]

### 2.3 Design rationale and practical implications

Efficient water transport and salt management are key to the systems that combine SIE with ion extraction. For the evaporation process, timely water transport to the evaporation surface is essential for effective heating and high-efficiency evaporation. During ion extraction, fast transport of ions to adsorption sites is crucial for efficient adsorption. Note that in extraction

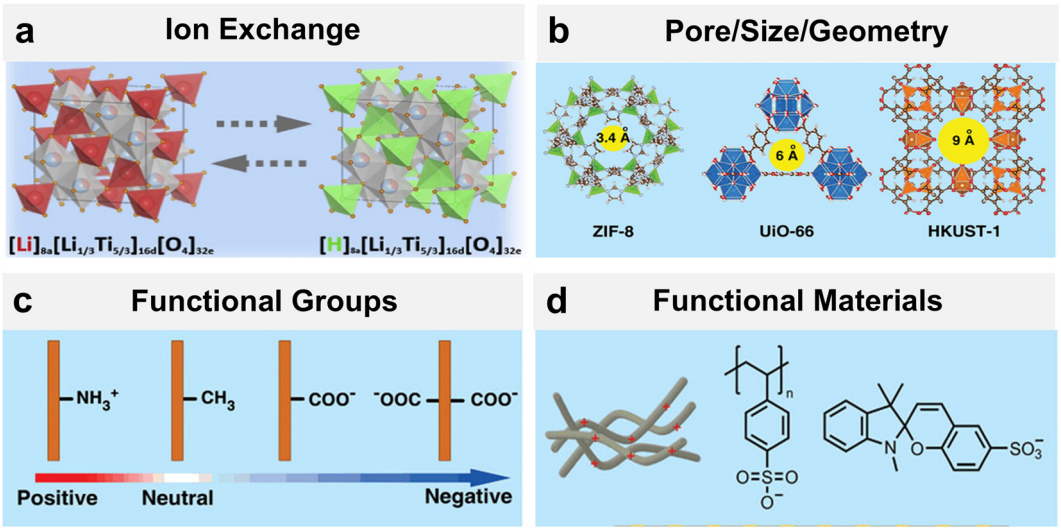


Fig. 3 Adsorption mechanisms and regulatory approaches of different materials. (a) is reproduced from ref. 54 with permission from Copyright (2024) Elsevier B.V. (b)–(d) are reproduced from ref. 20 with permission from Copyright (2024) John Wiley & Sons.

systems that do not use an adsorption mechanism, rapid mass transfer can also boost the ion extraction process and increase productivity.[14,58] Theoretical analysis has shown that transpiration flux, which is crucial to these processes, is primarily influenced by temperature.[59] Meanwhile, an increase in temperature can also accelerate the kinetics of ion adsorption and increase capacity, as explained by the Arrhenius equation and the Van't Hoff equation.[53] In light of this, an integrated SIE system with ion extraction capability is particularly effective, as it can utilize solar-thermal heat energy in a more efficient way, achieving high solar-to-thermal conversion and ion extraction efficiencies.

More importantly, considering real-world applications, the combination of SIE and ion extraction can also effectively reduce the discharge of highly concentrated brine into seawater during clean water production. This is crucial as increased seawater salinity poses serious environmental threats to aquatic life. Additionally, extracting ions during the SIE process presents a valuable approach to enhancing the versatility and viability of SIE for clean water production. Therefore, integrating clean water production with ion extraction during SIE is not only strategically beneficial but also maximizes the use of abundant solar energy. Such an integrated approach effectively addresses environmental concerns while providing a sustainable solution for water scarcity.

## 3. NaCl collection from brine during SIE

$Na^+$ is the most abundant ions in seawater and saline lake water. During the SIE of seawaters, $Na^+$ will diffuse and create concentration gradients. When the concentration reaches saturation, salt precipitation on the evaporation surfaces or other key components occurs, leading to salt scale buildup, which can potentially block the water pathway and reduce evaporation efficiency by obstructing light and hindering evaporation. To address the issue of salt crystallization during the SIE process, strategies such as salt circulation and salt discharge have been proposed.[60–64] Salt circulation aims to reduce salinity at the evaporation surface by enhancing convection between the evaporator and the bulk water. The salt discharge method involves managing brine transport to facilitate salt precipitation at specific locations, such as the edges of the evaporator, through deliberate structural design. However, not all these strategies can achieve ZLD because systems relying on the salt convection mechanism may allow some salt ions to return to the bulk brine.[65–68] This backflow can adversely affect the ecosystem and compromise water conservation and environmental protection efforts.[69,70] Additionally, when brackish water returns to the bulk water instead of being harvested, other valuable trace elements are lost.

ZLD is a wastewater treatment approach aimed at recycling or reusing all wastewater produced during the production process. It seeks to eliminate liquid discharge, leaving only solid salts as by-products.[71,72] Given global water shortages and resource scarcity, ZLD has gained significant attention for its potential to maximize resource recycling and minimize wastewater volumes. For the SIE system, effective ZLD can be achieved by optimizing the water delivery pathway to facilitate specific-site salt crystallization, thus maintaining clean solar-thermal and evaporation surfaces. Consequently, the salt precipitated at specific sites can be easily collected while ensuring a high clean water production rate. This section discusses strategies for achieving ZLD during clean water production and $Na^+$ extraction using SIE systems.

### 3.1 Specific-site salt crystallization

The specific-site salt crystallization in SIE systems is engineered to regulate salt precipitation by precisely controlling brine transport, thus effectively preventing salt formation on the

 

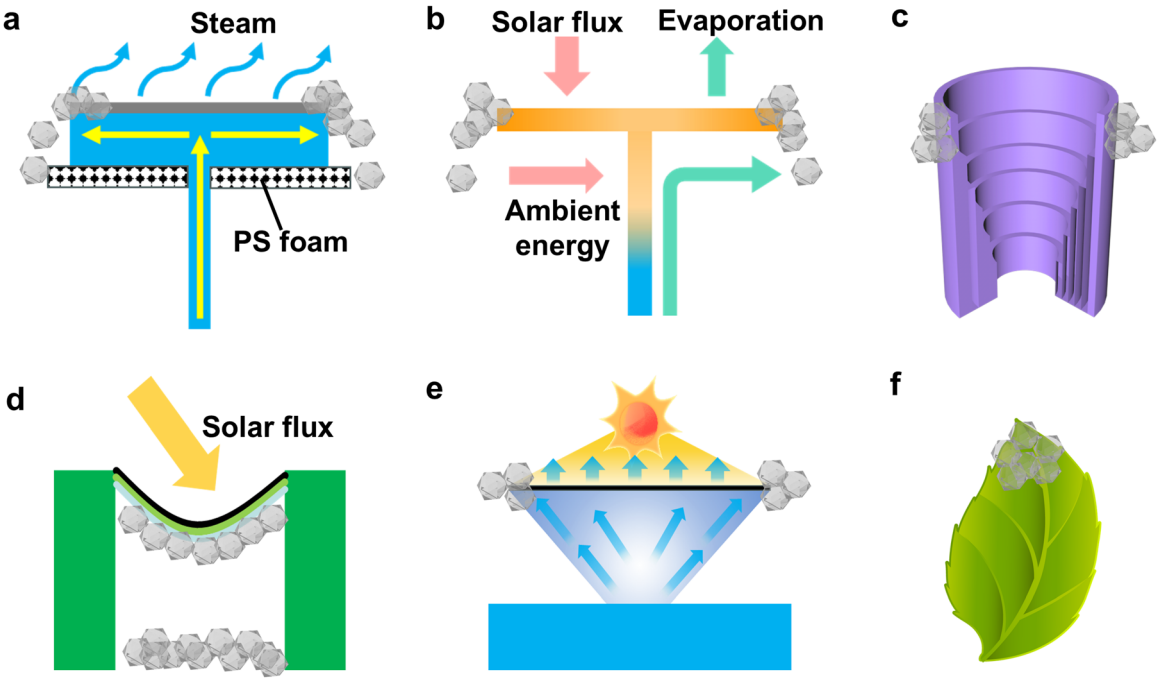


Fig. 4 Schematics strategies for specific-site salt crystallization. (a) 1D water transport path with heat insulation. (b) 1D water transport path with ambient energy absorption. (c) Spiral roll structure. (d) Suspended structure. (e) Conical frustum structure. (f) Biomimetic structure.

evaporation surfaces.[73–83] Various structures, ranging from flat to 3D, have been developed to create the desired salinity gradient and facilitate controllable crystallization (Fig. 4). These designs isolate salts from the solar-thermal and evaporation surfaces, helping to maintain stable evaporation performance.

**3.1.1 1D water transport path with heat insulation.** In SIE systems, the 1D water transport path facilitates the directional movement of water, while a thermal barrier layer provides heat insulation for effective thermal management. As the evaporation and water transfer processes progress, a salinity gradient develops from the center to the periphery of the evaporator, leading to a localized salt crystallization at the edge of the evaporator. Combining these structures enables specific-site crystallization and efficient heat management within a single solar evaporator system. Ye *et al.* designed a salt-rejecting solar evaporator with a unique T-shaped structure to facilitate directional water transport and targeted salt deposition.[84] This evaporator consists of three main components: a solar-thermal top layer made from commercial carbon black nanoparticles for high-efficiency solar absorption and solar-thermal conversion; a thermal barrier layer of expanded polyethylene foam, which provides flotation and heat insulation and a well-engineered directional water transport channel made from air-laid paper, allowing for efficient seawater delivery and directional brine drainage (Fig. 5a). Compared to traditional evaporation systems, where salts mostly accumulate on the solar-thermal layer, the design of the T-shaped structure can direct salts to deposit at the edges of the evaporation surface by optimizing water transport behaviour, simultaneously ensuring stable evaporation and facilitating salt recovery. Under 1 kW $m^{-2}$ solar illumination, the evaporator achieved an evaporation rate of 1.46 kg $m^{-2}$ $h^{-1}$ with a solar-thermal conversion efficiency of 91.7% and can operate effectively for 16 cycles without performance degradation. Zheng *et al.* introduced a honeycomb-like evaporator for efficient desalination and salt harvesting, enhanced by decorating the fabric with hydrophilic $Ti_3C_2T_x$ MXene (Fig. 5b).[78] The honeycomb structure, featuring concave arrays, improves the light absorption efficiency through multiple scattering and multi-angle light absorption. This evaporator also exhibits 1D water transport path that reduce heat loss and concentrate heat on the surface, enabling highly efficient evaporation. More importantly, when the 1D water transport path is centered within the evaporator, it generates a radial concentration gradient from the center to the edges, causing salt to crystallize at the edge of the evaporator selectively. The evaporator achieved a high energy efficiency of up to 93.5% and an evaporation rate of 1.62 kg $m^{-2}$ $h^{-1}$ under one sun irradiation, and it also allowed complete water/solution separation and convenient salt collection. In another experimental study, an innovative one-way brine-flowing evaporation system was designed by growing polypyrrole onto glass fiber, which successfully achieved high production of both steam and salts by utilizing solar energy and waste heat.[77] Systematic investigations revealed the effects of salt concentration and ionic species on evaporation and salt generation behaviors (Fig. 5c). During the evaporation of a 10% NaCl solution under varying light intensities, it was observed that the radius of the crystalline salt rings decreased as the light intensity increased.

Similarly, when evaporation occurred in sunlight with varying concentrations of NaCl solutions, the radius of crystalline rings also decreased with increasing salt concentration. It is understood

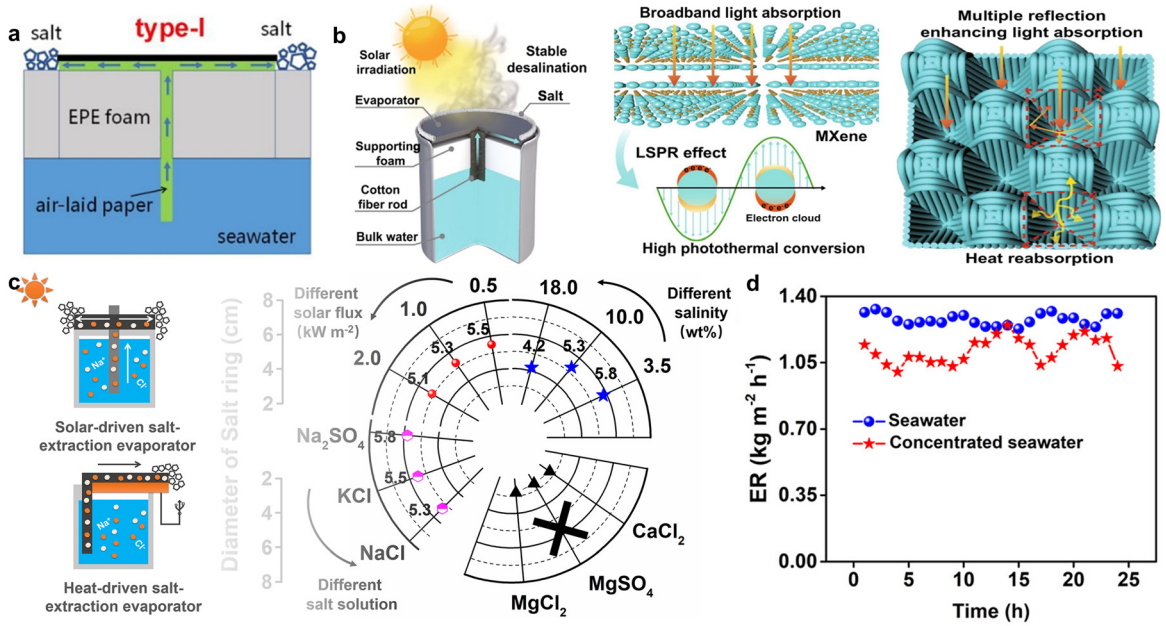


Fig. 5 (a) Salt-rejecting solar evaporator with 1D water transport channels and heat resistance layer. Reproduced from ref. 84 with permission from copyright (2020) American Chemical Society. (b) Schematic diagram of an MXene-decorated 3D honeycomb fabric-based solar evaporator for desalination based on the LSPR effect of MXene and the 3D honeycomb-structured fabric. Reproduced from ref. 78 with permission from copyright (2021) Springer Nature. (c) Illustration of the water and salt transport system along with the measurement of salt rings under different conditions. (d) The evaporation rate of the solar-driven salt-extraction evaporator in seawater and concentrated seawater. Reproduced from ref. 77 with permission from copyright (2024) Elsevier.

that greater solar intensity, higher initial salt concentration and shorter time for NaCl to reach saturation all contributed to a smaller radius of the resulting crystalline circle. This evaporator facilitated the evaporation of concentrated seawater at an average rate of 1.12 kg $m^{-2}$ $h^{-1}$, producing 4.21 g of salts over 24 hours under standard sunlight. Under an elevated temperature of 60 °C, a stable, high evaporation rate of 2.58 kg $m^{-2}$ $h^{-1}$ was achieved, yielding 12.92 g of salts during a continuous 30-hour operation (Fig. 5d). It is worth noting that while adding additional insulation components significantly reduces heat loss, it also reduces the exposure area of the evaporation surface, potentially limiting the evaporation rate.

**3.1.2 1D water transport path with ambient energy gain.** By removing the insulating layer and inserting the bottom of the 1D water transfer channel directly into the water, the air between the evaporator and bulk water can be used directly as an insulating layer. This approach allows the harnessing of convection currents and ambient energy, significantly improving the water evaporation performance of the evaporator. Xue *et al.* demonstrated a synthetic tree-like structure through unidirectional freeze-casting of a polyvinyl alcohol matrix and subsequent polypyrrole decoration to simultaneously achieve high steam productivity, environmental energy harvesting, edge-preferential crystallizing and efficient salt collection (Fig. 6a).[85] The anisotropic vertical pores formed during the freeze-casting process create 1D water transport paths, enabling rapid water transport while reducing heat loss during SIE. Meanwhile, as water evaporating, salt crystallized preferentially at the edge of the evaporation disc, preventing salt accumulation within the evaporation system and minimizing brine flow back, thereby reducing disruption to natural ecosystems. When exposed to sunlight, the synthetic tree-like evaporator achieved an evaporation rate of 2.03 kg $m^{-2}$ $h^{-1}$ and a salt collection rate of 59.879 g $m^{-2}$ $h^{-1}$, with a solar thermal efficiency of 75%. This evaporator operated steadily over 60 hours with continuous salt crystallization, demonstrating long-term durability. Cheng *et al.* developed an evaporator featuring a Janus-based directional salt transfer structure, enabling stable evaporation in high-salinity solutions while simultaneously recovering salts.[86] This evaporator uses a polytetrafluoroethylene/polypyrrole-decorated sponge as the absorber, with a piece of polystyrene foam as the thermal insulation layer and supporting substrate (Fig. 6b). Assisted by a 1D hydrophilic carbon felt water path in the center, the salt solution transported in the evaporator generates a radial concentration gradient from the center to the edge, trapping salts beneath the upper surface of the absorber. As a result, the salts precipitated only at the edges and eventually fell off under gravity, enhancing the ZLD capability of the system. An evaporation rate of 18.63 kg $m^{-2}$ $day^{-1}$ was achieved in 20 wt% NaCl solution. However, challenges exist with long-term evaporation, as salt crystals can still accumulate and block water transport channels due to insufficient vertical brine loading and poor design of the 1D water transport path.

**3.1.3 3D structure design for specific-site salt crystallization.** Due to the limitations of the transmission capacity in the 1D water transmission path, there is a tendency for salt crystals to accumulate. This has led to the development of SIE

 

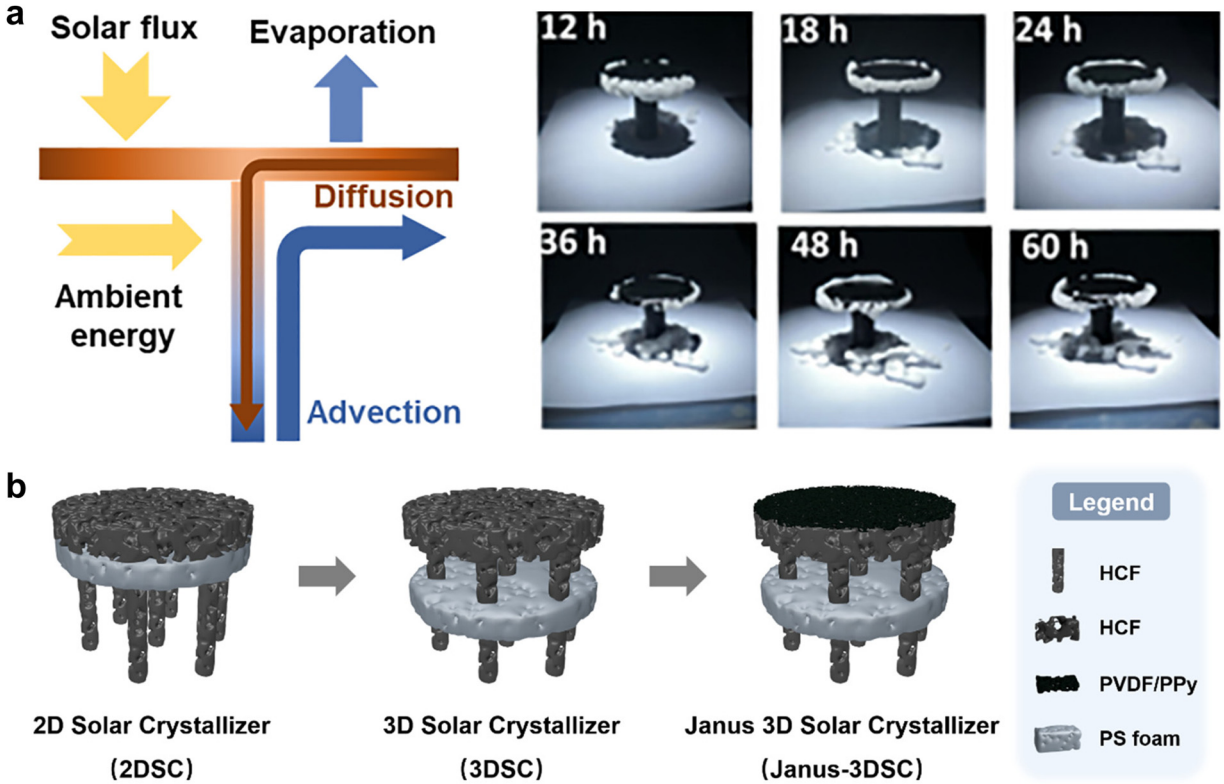


Fig. 6 (a) Schematic illustration of the bioinspired synthetic tree for solar steam generation and salt collection and photographs of salt collection over 60 hours under 1 sun. Reproduced from ref. 85 with permission from copyright (2024) John Wiley & Son. (b) Schematic of a Janus-based interfacial solar evaporator. Reproduced from ref. 86 with permission from copyright (2024) Elsevier.

systems with 3D structures. The rapid directional transport capability and intrinsic anti-clogging properties of the 3D specific-site salt crystallization structure offer promising avenues for the development of advanced evaporators. Additionally, the 3D architecture enables efficient energy recovery from the surrounding environment while creating an expanded vapor-to-liquid interface to facilitate enhanced steam release. For example, a 3D porous graphene spiral roll (3GSR) evaporator was constructed from a porous melamine film with a gradient structure decorated with graphene oxide/cellulose nanocrystals, which increases in height from the inner to the outer edge.[87] This gradient design allows for a gradual increase in brine concentration within the evaporator, flowing from the bottom to the top, facilitating crystallization at specific sites (Fig. 7a). The 3GSR design can promote energy recovery, radial brine transport and directional salt crystallization, achieving an exceptionally high evaporation rate of 9.05 kg $m^{-2}$ $h^{-1}$ in 25 wt% brine solution under 1-sun illumination and an impressive salt collection rate of 2.92 kg $m^{-2}$ $h^{-1}$. Deng *et al.* proposed a suspended-type evaporator (STE) utilizing Janus fibrous mats for salt-resistant solar desalination and mineral recovery.[88] The top solar-thermal layer of the STE was created by filtering and spreading carbon nanotubes onto biodegradable cellulose acetate fibrous mats, followed by coating polydimethylsiloxane to enhance hydrophobicity. Polyacrylonitrile fibers were added to the opposite side to form a hydrophilic evaporation layer. The configuration simultaneously achieves excellent salt resistance, efficient evaporation and salt recovery due to several key features: (1) the upper hydrophobic solar-thermal-evaporation layer can effectively absorb light and facilitate water evaporation, while the lower hydrophilic layer is designed to induce salt crystallization; (2) in this Janus structure, salt enrichment and crystallization are confined to the bottom hydrophilic layer, preserving the integrity of the hydrophobic solar-thermal-evaporation layer and ensuring uninterrupted evaporation performance and easy salt harvesting; (3) such design also provides additional low-resistance vapor escape paths, allowing vapor to exit directly from the evaporation layer into the atmosphere unlike traditional floating Janus evaporators (Fig. 7b). As a result, the designed evaporator exhibited a stable evaporation rate of 1.94 kg $m^{-2}$ $h^{-1}$ and demonstrated ZLD salt resistance with optimal mineral recovery. A 3D cone-shaped structure made from polyvinyl alcohol hydrogel was designed to facilitate localized salt crystallization for desalinating high-salinity brine, taking advantage of the characteristics of a conical frustum.[89] To improve light absorption, the top surface of the hydrogel is covered with an MXene-fibre-cloth (Fig. 7c). This design endows the hydrogel with excellent water transport capability and brine transport management that enable salt redissolving during desalination. As the cross-sectional area of the conical frustum increases, it promotes radial brine transport, leading to the highest salt concentration at the edge of the evaporator.

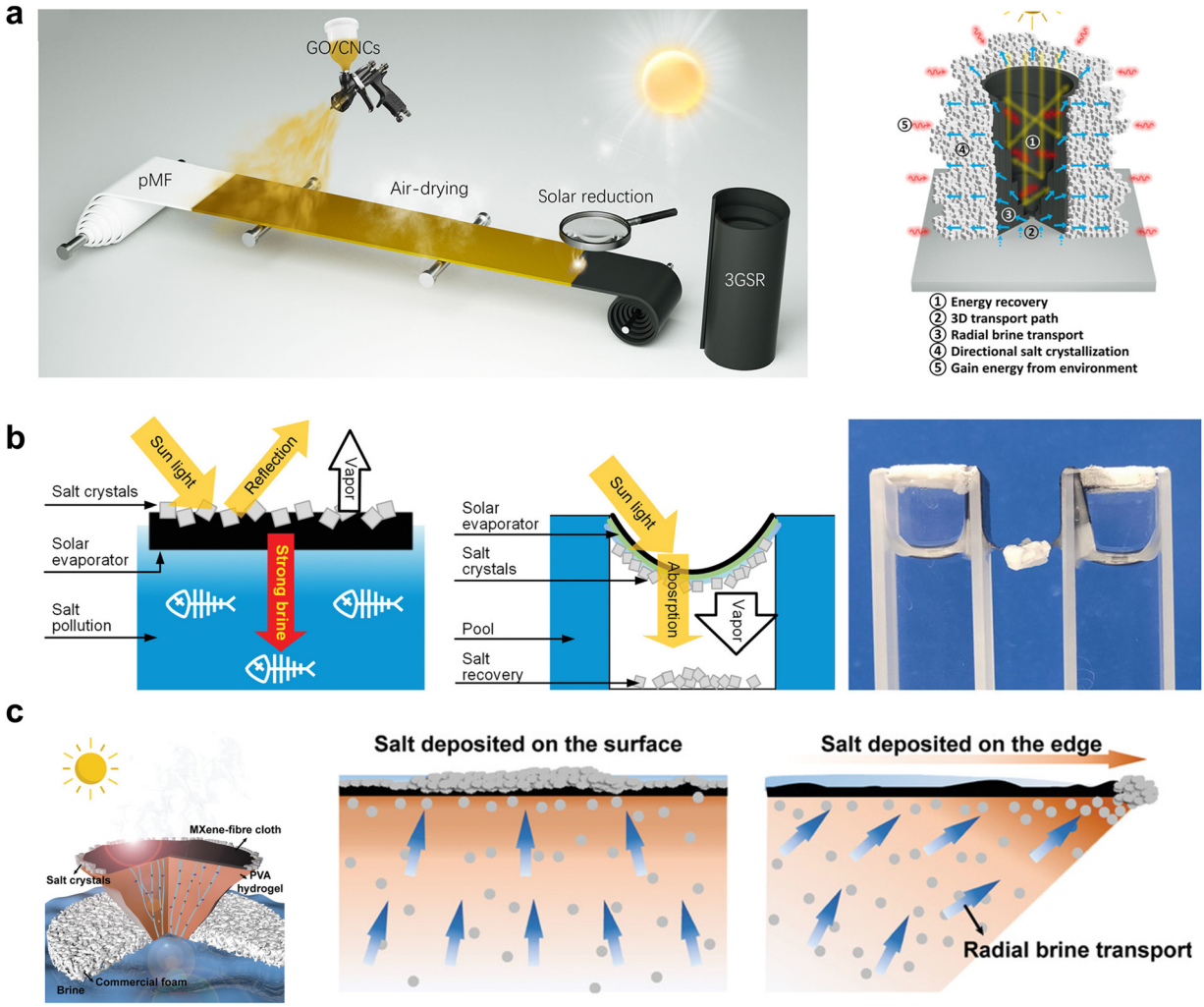


Fig. 7 (a) The process of fabricating 3GSR and its efficient SIE and salt collection by directional salt crystallization. Reproduced from ref. 87 with permission from copyright (2024) John Wiley & Sons. (b) Comparison of salt crystallization and the high-concentration brine discharge in the traditional solar evaporator and the suspended type evaporator. Reproduced from ref. 88 with permission from copyright (2024) John Wiley & Sons. (c) Comparison of salt crystallization in conventional evaporator and cone-shaped structure with radial brine transport. Reproduced from ref. 89 with permission from copyright (2024) John Wiley & Sons.

In contrast, when the evaporator has a cylindrical shape, it directs wetting from the outer edge toward the center, resulting in the highest salt concentrations at the center and leading to preferential salt deposition on the main surface, which can obstruct light absorption and impede vapor escape. The edge of the cone-shaped evaporator continuously removed salt at an average rate of at an average rate of 2.07 kg $m^{-2}$ $h^{-1}$ from brine containing 10 to 25 wt% NaCl. This process maintained steady performance under one sun irradiation and can operate continuously for 24 hours.

**3.1.4 Bionic structural design for specific-site salt crystallization.** Nature offers a vast source of inspiration for material design. For example, inspired by mangrove, a salt-tolerant plant known for its efficient salt management, multifunctional evaporators have been developed to mimic mangrove functions.[90] This innovative all-in-one device facilitates direct solar vapor generation and allows for salt collection without discharging brine. It incorporates artificial leaves where the edges serve as the evaporation surface for vapor release, while a hydrophilic stem supplies water continuously through capillary wicking (Fig. 8a). The efficiency of the device is further enhanced by a nano/micro-structured titania layer created through chemical etching on titanium mesh. In this study, a systematic investigation was explored factors such as the tilt angle of the leaf and the height of the stem, which affect the evaporation performance and salt crystallization behaviors of the evaporators. Trials indicate that a tilt angle of 30 degrees, coupled with longer stems, significantly boost performance by enhancing salt harvesting and liquid-wicking capabilities. During desalination in the daytime, the precipitated salt, which exhibits a porous nature, accumulates at the edges of the leaves because of the weaker capillary forces at those locations. At night, rehydration of the leaves by saline water and the influence of gravity cause the salt to peel off, establishing a sustainable

 

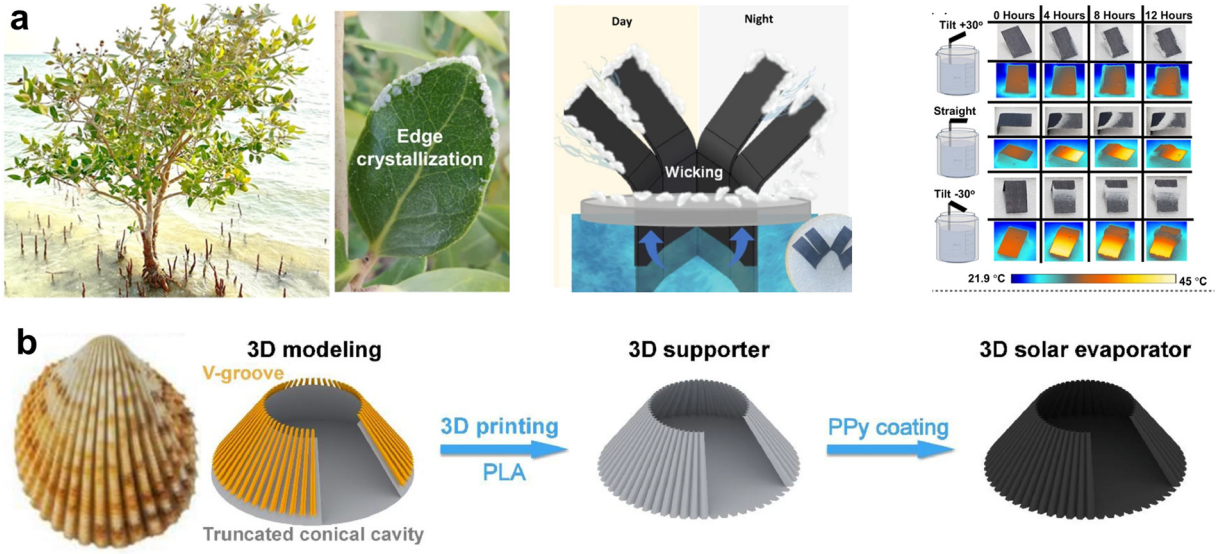


Fig. 8 (a) Mangrove-inspired evaporator for specific-site crystallization. Reproduced from ref. 90 with permission from copyright (2024) Springer Nature. (b) Vasticardium vertebratum-inspired evaporator for specific-site crystallization. Reproduced from ref. 91 with permission from Copyright (2024) Elsevier B.V.

day/night cycle for the co-production of clean water and salt. Notably, the salt patches can increase vaporization rates by up to 1.6 times, ensuring that salt accumulation on the evaporation surface does not impede overall evaporation rates. The proposed solar vapor generator demonstrated a stable solar-thermal efficiency of approximately 94% in 3.5 wt% brine under standard sunlight conditions. In outdoor settings, it can produce 2.2 L of clean water per square meter per day from seawater, which is sufficient to meet individual drinking water needs. Another creative design is inspired by the shell ornamentation of the Vasticardium vertebratum, whose outer shell surface exhibits radially arranged grooves and spine-bearing ridges. Tian *et al.* designed a spined groove-ridge pair with a sea-shell-mimetic radial V-groove array for rapid and directional water transport, realized through 3D printing and *in situ* polypyrrole polymerization (Fig. 8b).[91] The grooves reduce resistance and enhance water flow, while the spines on the ridge facilitate rapid salt transfer. Meanwhile, the hollow, truncated cone-shaped enclosure enhances stability and enables localized heating, achieving highly efficient water evaporation with approximately 95% efficiency. The radial groove and ridge structure not only recover diffuse reflected light energy and radiative heat loss but also promote localized salt crystallization at the top edge of the evaporator, which is attributed to the integration of liquid and solid delivery systems. The two-in-one integration design of the 3D evaporator offers improved performance, enabling superior solar-driven ZLD and excellent long-term salt resistance, even when desalinating high-salinity brine (20 wt% NaCl) and various heavy metallic salt solutions.

### 3.2 Preventing salt adhesion on the evaporator surface

During the SIE process, if salt crystals adhere strongly to the surface of the evaporator for an extended period, they can reduce both evaporation rates and evaporation efficiencies while also impeding the easy collection of salt crystals. Traditional strategies, such as continuously scraping off salts and using gravity for salt removal are straightforward but often face limitations, particularly when addressing microscale salt contamination or preserving delicate surface structures. Typically, strong adhesion of salt crystals to the evaporator surface occurs due to the large contact area between the solid surfaces. The development of evaporators with surfaces that exhibit ultralow adhesion to salts is a promising strategy for enhancing the efficiency of SIE systems and achieving ZLD. Efforts have been made to weaken the adhesive forces between the salt grains and the evaporation surface, which allows the grains to move more freely and detach easily under gentle airflow. For example, coating the evaporator surface with oil has proven effective in achieving ultralow salt adhesion.[92–96]

An evaporator (PLIS-1) with an engineered lubricant-infused surface structure (CSL) was created using candle soot deposition, polydimethylsiloxane (PDMS) dip coating and lubricant impregnation.[97] The PDMS can stabilize the candle soot by forming superhydrophobic PDMS-coated candle soot particles, which were then infused with lubricant oil *via* spin-coating (Fig. 9a). This design enables a full-wave band absorbance of 97%, attributed to the high light absorption properties of CSL and also ultra-low adhesion with salt crystals (2 mN $mg^{-1}$), which is much lower than that observed on a rubber surface (80 mN $mg^{-1}$) (Fig. 9b).[98,99] In addition, the lubricant layer increases the nucleation barrier, allowing only a limited number of salt crystals to form on the surface. As evaporation progresses, these crystals migrate inward, resulting in densely packed crystal formation, which minimizes extensive solid–solid contact with the evaporation surface. Consequently, salt crystals can be easily detached by applying a gentle airflow (Fig. 9c).

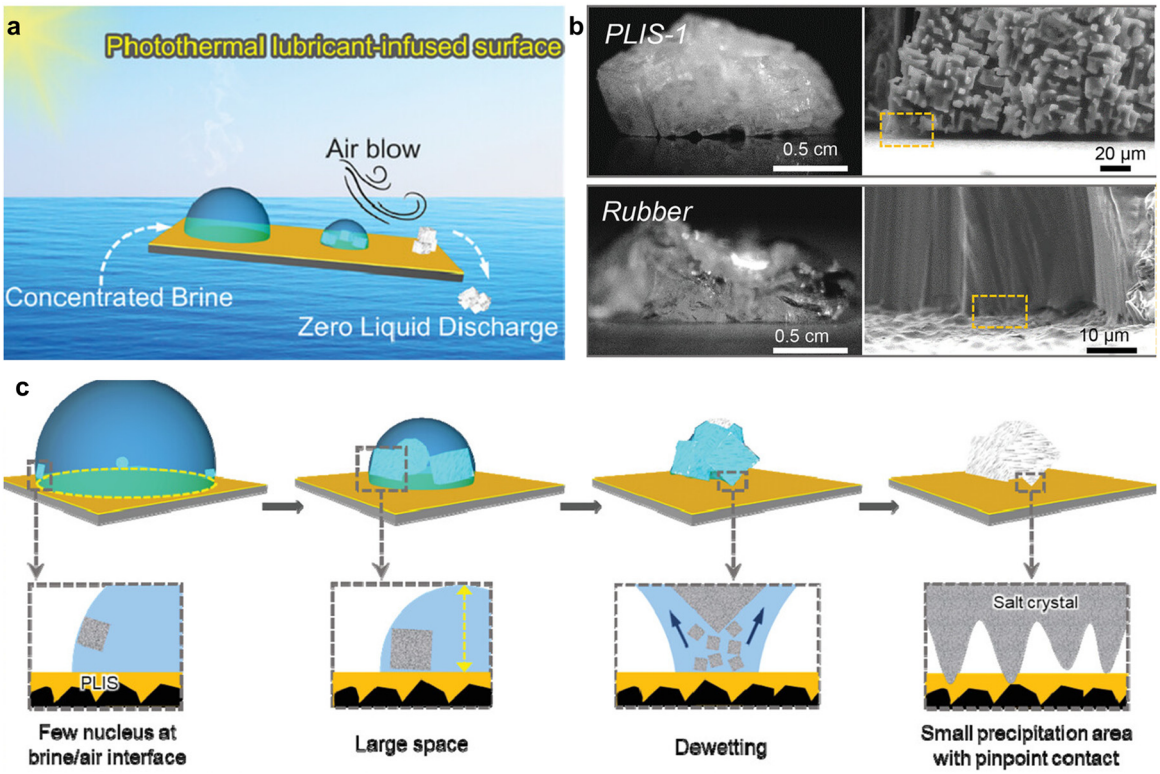


Fig. 9 (a) Schematic illustration of the novel solar-thermal lubricant-infused surface for hypersaline brine desalination. (b) Side-viewing SEM images of salt crystals formed by brine droplet evaporation on the PLIS-1 and rubber surface. (c) Mechanism of the salt crystallization on the PLIS surface. Reproduced from ref. 97 with permission from copyright (2024) John Wiley & Sons.

This lubricant-interface-induced mobile crystallization strategy offers a promising approach for treating hypersaline wastewater with ZLD. In another study, an evaporation disc was created using a layer-by-layer approach, consisting of a horizontal evaporation surface and a vertical solution uptake thread.[75] This configuration allows for controlled transport and distribution of the salt solution within the solar-thermal material, facilitating simultaneous steam generation and salt harvesting from hypersaline sources. The uptake thread, inserted at the center of the disc, can also create a radial concentration gradient from the center to the edge, enabling salt to crystallize only at the edge of the disc, which effectively minimizes disruption from salt accumulation during the evaporation process. Prewetting the disc in dark conditions can effectively disrupt the dynamic equilibrium between crystallization and dissolution, significantly weakening the interactions between salt crystallization and the evaporation surface. Thereby, salt crystals can detach and fall off solely from the evaporator due to gravity without requiring additional interventions. Peng *et al.* reported a novel programmable solar-thermal textile umbrella engineered for efficient desalination and salt harvesting, achieved through the asymmetric deposition of $MoS_2$ nanosheets combined with multi-scale structural design. The reduced binding forces between the umbrella and salt crystals enable controllable, edge-preferential salt crystallization and gravity-assisted salt harvesting.[100]

### 3.3 Separation of solar-thermal material and evaporation surface

Separating the solar-thermal material from the evaporation surface represents another viable approach to mitigate the issue of salt crystal formation on the solar-thermal and evaporation surfaces during operation, ensuring constant solar absorbing effectiveness and stable evaporation performance. This separation can avoid direct contact between solar-thermal materials and brines, thereby effectively preventing the deposition of salt crystals on the solar-thermal surfaces. Furthermore, it allows for precise control over the processes of water evaporation and salt crystallization, facilitating easier salt collection.

Gu *et al.* presented a paper-based thermal radiation-enabled evaporation system (TREES) that exhibits vertical evaporation walls around the perimeter and a light-absorbing layer at the bottom, designed for sustainable and highly efficient salt-collecting desalination (Fig. 10a).[101] The separation of the evaporating wall from the bottom light-absorbing material prevents the formation of salt crystals on the surface of the light-absorbing materials, thus maintaining their absorption capacity during evaporation. Additionally, the walls can block thermal radiation from the heated bottom, while the side surfaces can absorb environmental energy, contributing to the evaporation performance of the system (Fig. 10b). When treating 7 wt% brine, this TREES system achieved a stable evaporation rate of 2.25 kg $m^{-2}$ $h^{-1}$ under one sun illumination while enabling continuous salt generation and collection (Fig. 10c).

 

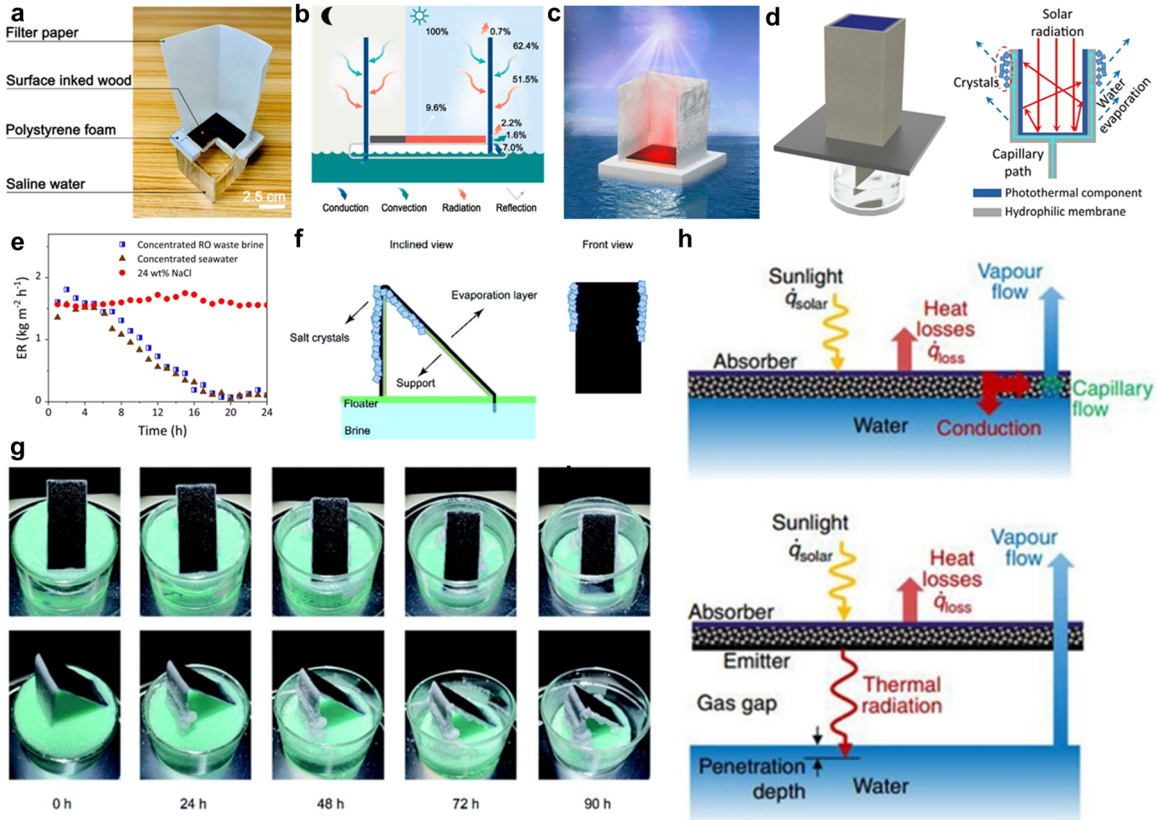


Fig. 10 (a) Photo of the cross-sectional view of a TREES. (b) Energy balance of TREES with a height of 15 cm. (c) Schematic showing day and night uninterrupted desalination *via* TREES. Reproduced from ref. 101 with permission from copyright (2020) American Chemical Society. (d) Schematic illustration of solar crystallization device. (e) The evaporation rate of 24 wt% NaCl brine and natural seawater brine in the 24-hour operation. Reproduced from ref. 72 with permission from copyright (2021) Springer Nature. (f) Schematic illustration of the 3D solar crystallizer. (g) Photographs of the two water transportation layers-crystallizers at different solar brine evaporation times. Reproduced from ref. 102 with permission from copyright (2024) Royal Society of Chemistry. (h) Comparison of two different evaporation structures. Reproduced from ref. 103 with permission from copyright (2018) Springer Nature.

Separating the light-absorbing surface from the evaporation surface can effectively reduce the degradation of solar-thermal water evaporation performance caused by undesired salt deposition. However, this spatial separation may also hinder the timely transfer of heat to the evaporation surface, potentially resulting in less-than-optimal performance. Wang *et al.* reported a hierarchical 3D SIE structure that increases evaporation efficiency and reduces heat loss through a dead-end type solar-driven water evaporation mode.[72] In this setup, an outer wall serves as the surface for water evaporation and salt crystallization, while an inner wall, consisting of a light absorption component, is used for solar-thermal conversion (Fig. 10d). An aluminum sheet with high thermal conductivity effectively connects the water evaporation and light absorption surfaces, enabling efficient heat transfer. Thanks to these features, the evaporation device achieved a high evaporation rate of 1.61 kg $m^{-2}$ $h^{-1}$ under one sun illumination while treating concentrated brine containing 24 wt% NaCl (Fig. 10e). Two units are often required in the designs mentioned above: one for solar absorption and another for water evaporation. Additionally, it is necessary to adjust the hydrophilicity or hydrophobicity of the materials used for solar-thermal conversion and water transportation processes. This requirement further adds complexity to both the preparation process and the structural design. To achieve both high water purification and salt collection efficiencies, Xu *et al.* proposed a novel approach by creating separate areas for solar evaporation and non-solar evaporation, effectively isolating the water evaporation surface from the salt crystallization surface.[102] This design utilizes a solar-thermal evaporation layer made by coating reduced graphene oxide onto commercial bamboo fiber paper with sodium alginate as a binder. Unlike designs that require multiple components, this approach uses a single material structure supported adequately to maintain separation (Fig. 10f). The system exhibits an inclined evaporation surface oriented towards the sun to maximize radiation absorption alongside a vertical crystallization surface that facilitates natural, dark evaporation and allows for salt ion accumulation (Fig. 10g).

It has been demonstrated that direct contact between the water and the evaporators leads to fouling while maintaining the vapor temperature near the boiling point, which would lead to unsatisfactory evaporation rates. In contrast, the application of physical and thermal separation designs can prevent pollution and blockages, which not only enhances the stability and contamination resistance of the evaporator but also enables the

production of superheated steam at 133 °C in a non-pressurized system under one sun illumination. Furthermore, using the high infrared absorbency of water to capture infrared energy from heating objects proves to be an effective method. This approach facilitates the separation of the evaporation surface from the absorption surface, thereby optimizing performance. Liu *et al.* designed a solar-thermal-radiative evaporator with a solar-thermal converter that captures and converts the full-band solar energy into infrared radiation to heat conical porous materials.[104] The proposed design spatially separates the solar-thermal converter from the evaporation surface, isolating salt crystallization from the water evaporation process and facilitating salt recovery through gravity. This allows radiation and natural evaporation to function independently, enhancing both solute transport and vapor diffusion. As a result, the system maintained a high evaporation rate of 1.25 kg $m^{-2}$ $h^{-1}$ with a solar efficiency of 89.9% under one sun illumination over 40 hours while simultaneously enabling clean water and salt collection. Chen *et al.* developed a contactless SIE structure that utilizes strong infrared absorption properties and physically separates the absorber from the water (Fig. 10h).[103] The evaporator can operate effectively in 3.5 wt% brine over extended periods without any observable salt crystallization. Finally, Fig. 11 provides a comparative analysis of strategies for NaCl collection during the SIE process. The selection of appropriate strategies must be meticulously balanced with the specific requirements of each application, taking into account factors such as long-term system stability, cost-effectiveness, efficiency, and ease of maintenance.

# 4. Extraction of low-concentration ions during SIE

Seawater and brine contain a variety of valuable ions, which are in demand for their excellent physicochemical properties in various applications.[105–109] Nonetheless, the separation and collection of these ions are complicated by their low concentration and the presence of interfering ions in high concentrations.[110–118] Recent strategies for the synchronous extraction of low-concentration ions from water during the SIE process fall into three main categories: ion adsorption, sequential and separable crystallization of cation species based on their concentrations and solubilities and membrane separation. While adsorption methods have shown potential for increasing ion recovery from low-concentration sources, they are still hindered by limited adsorption capability and the need for chemical usage. Alternatively, a method that leverages the high solubility and mobility of ions in water has been proposed for the rapid and selective extraction of ions from saline water.[14] However, the reliance of this method on long-distance ion migration presents significantly challenges for device fabrication. Another viable approach involves using an ion separation membrane combined with a solar evaporator for direct ion extraction from salt-lake brines.[58] This system features a multilayer structure with an upper solar-thermal layer designed to evaporate water, a hydrophilic porous membrane in the middle that generates capillary pressure to drive water transport and a very thin ion separation membrane at the bottom that allows specific target ions to pass while blocking other multivalent ions. Combining size sieving and Donnan exclusion in nanofiltration membranes effectively separates monovalent and divalent ions.[119] This section provides a detailed discussion, comparison and analysis of the principles underlying these strategies.

## 4.1 Ion adsorption

**4.1.1 Organic adsorbents.** Among all adsorption materials, organic adsorbents are the closest to feasible large-scale deployment. The organic absorbents generally include polymers,[120] covalent organic frameworks (COFs)[121,122] and MOFs.[123,124] Organic materials can be rationally engineered to enhance their selectivity for trace ions, particularly in complex mixtures containing multiple metal ions. By fine-tuning their chemical structures or composite architectures, the adsorption performance of these materials can be optimized. Many organic materials also exhibit excellent regeneration capabilities, enabling repeated use and reducing costs while simultaneously supporting the principles of sustainable SIE technology. Additionally, materials such as MOFs are characterized by exceptionally high surface areas, providing abundant adsorption sites to improve ion capture capacity. Their large surface areas

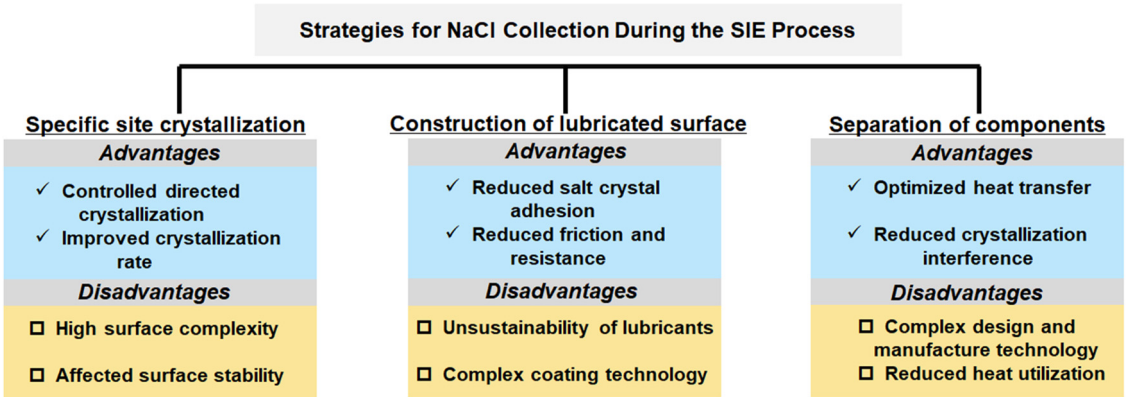


Fig. 11 Comparison of the strategies for NaCl collection during the SIE process.

 

further promote solar light absorption, enhance the vapor–liquid interface and accelerate vapor generation processes.

A bifunctional graphene aerogel (BHMS) assembled using bayberry tannin (BT) has been developed for SIE and marine uranium extraction.[125] The introduction of BT not only boosts the solar thermal conversion efficiency of the aerogel but also improves its uranium binding capacity. Additionally, the hydrophilic nature of BT enhances fluid infiltration within the aerogel matrix, leading to more effective SIE. Meanwhile, transpiration-induced steam generation can promote the adsorption of uranium ions, aiding in uranium extraction. This system can generate steam at a rate of 1.80 kg $m^{-2}$ $h^{-1}$ with a high energy efficiency of 95.5% under solar illumination while also enabling uranium to reach a concentration of 230.10 mg $g^{-1}$ within six hours. Qiu *et al.* also designed a porous polymer scaffold made from polydimethylsiloxane, which was functionalized with COFs to create an efficient solar desalination and selective uranium recovery system (Fig. 12a).[126] This scaffold with a hierarchical open porous structure can effectively transport water, enable increased evaporation sites and provide selective binding sites for uranyl, achieving a high evaporation rate of 1.39 kg $m^{-2}$ $h^{-1}$ and a uranium recovery capacity of 5.14 ± 0.15 mg $g^{-1}$ under sunlight. Additionally, the COF hydrogel was developed for simultaneous seawater desalination and uranium extraction,[127] displaying an evaporation rate of 0.744 kg $m^{-2}$ $h^{-1}$ and a uranium extraction capacity of 4.15 mg $g^{-1}$. The hydrogel matrix serves as the key component of the evaporator, offering efficient water transport paths and multiple bonding sites for uranyl ions. The presence of hydroxyl and thiazole rings within the COF skeleton further enhance its function as an adsorbent, making it particularly effective for the selective extraction of uranyl.

Inspired by the water transpiration and nutrient transport mechanisms of Salvinia cucullate, Wang *et al.* engineered a green tea waste/graphene aerogel (GDT) with Salvinia cucullate root-like structures and solar-thermal properties for uranium capture (Fig. 12b).[17] The design of the aerogel displays a highly porous structure containing rich active adsorption sites,

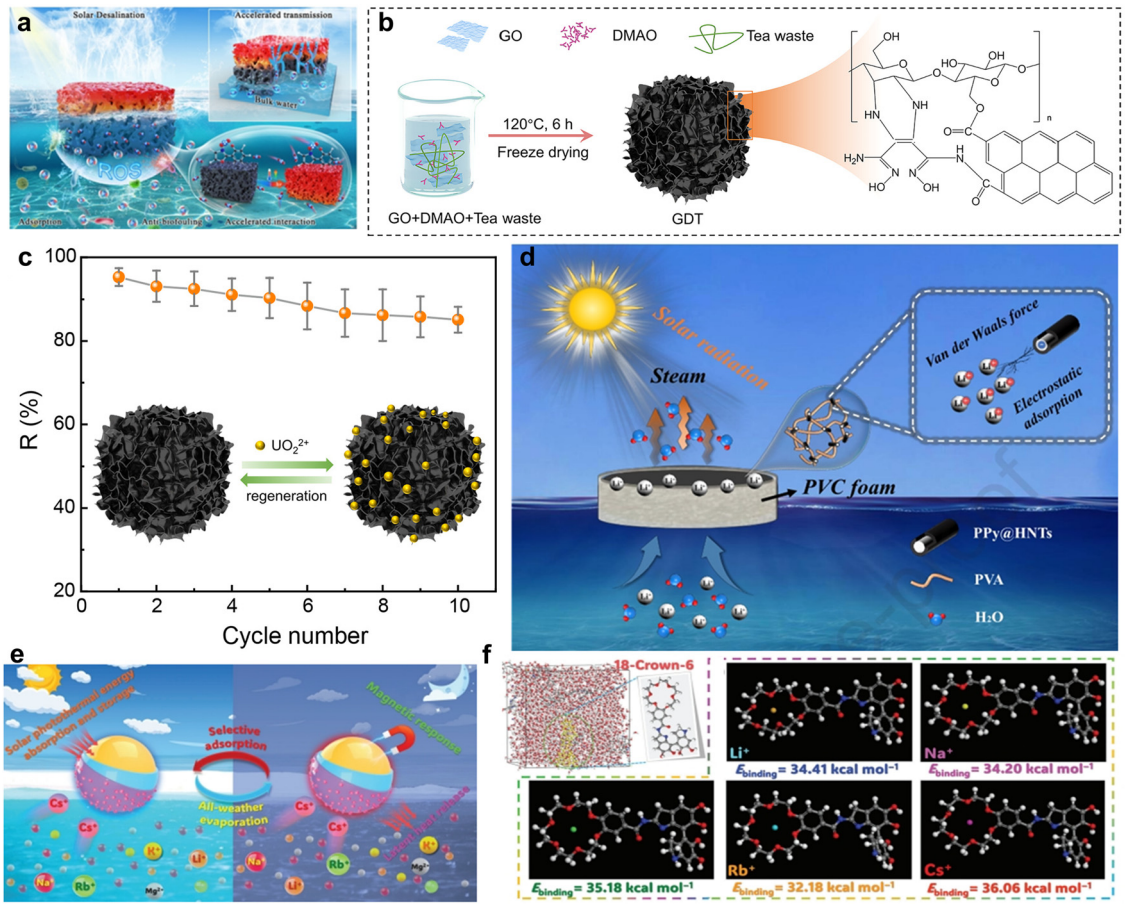


Fig. 12 (a) Schematic depicting BHMS sponge for synergistic solar desalination and uranium recovery. Reproduced from ref. 126 with permission from copyright (2021) American Chemical Society. (b) Diagram of GDT synthesis procedures. (c) Regeneration efficiencies of GDT in ten adsorption/desorption cycles. Reproduced from ref. 17 with permission from Copyright (2024) Elsevier B.V. (d) Schematic diagram of the evaporative and sorption mechanism of PPy@HNTs/PVA hydrogel. Reproduced from ref. 128 with permission from Copyright (2024) Elsevier B.V. (e) Scheme of all-weather solar-powered desalination and synchronous $Cs^+$ extraction for salt-lake water enabled by Crown-MicPCM. (f) A representative snapshot of the simulation model and snapshots for 18-Crown-6/$Li^+$, 18-Crown-6/$Na^+$, 18-Crown-6/$K^+$, 18-Crown-6/$Rb^+$, and 18-Crown-6/$Cs^+$ simulation systems and their $E_{binding}$ in a single solution. Reproduced from ref. 105 with permission from copyright (2024) John Wiley & Sons.

enhancing its adsorption capacity while accelerating mass transfer. Additionally, the incorporation of green tea waste improves the antibacterial and antifouling properties of the aerogel due to the bacteria-inhibiting effects of tea polyphenols and saponins. Furthermore, the aerogel is modified with amidoxime-functionalized diaminomaleonitrile, which boosts uranium adsorption capacity and selectivity. When tested in natural seawater, the aerogel evaporator demonstrated a high water evaporation rate (2.72 kg $m^{-2}$ $h^{-1}$) and a high uranium extraction capacity of 11.9 mg $g^{-1}$ with remarkable selectivity and high reusability of 85.1% after 10 cycles of adsorption-regeneration (Fig. 12c). Yang *et al.* designed a polypyrrole@halloysite nanotubes/polyvinyl alcohol (PPy@HNTs/PVA) hydrogel optimized for efficient SIE and rapid lithium sorption, benefiting from its full-spectrum light absorption and low evaporation enthalpy (Fig. 12d).[128] The HNTs embedded in the hydrogel can adsorb $Li^+$ ions, while PPy enhances the light absorption and solar-thermal conversion capability. The rich surface oxygen-containing functional groups of the hydrogels can interact with water molecules to break the hydrogen bonds in water, thereby reducing the evaporation enthalpy. This unique design enabled a high evaporation rate of 2.97 kg $m^{-2}$ $h^{-1}$ with an energy efficiency of up to 93.2% and allowed the hydrogel to reach $Li^+$ ion sorption equilibrium within 5 minutes.

Recently, a novel DNA hydrogel evaporator has been developed to enhance water evaporation and target metal ion adsorption following the above-mentioned design principle.[129] The DNA hydrogel creates substantial amounts of intermediate water within its matrix, reducing the energy required for evaporation.[130,131] Meanwhile, DNA structures in the hydrogel can selectively bind metal ions, enhancing uranium capture from seawater with a capacity of 5.7 mg $g^{-1}$ and a selectivity ratio 10.4 times greater than for vanadium, coupled with a high evaporation rate of 3.54 kg $m^{-2}$ $h^{-1}$. In another study, a nanostructured hydrogel solar evaporator was prepared by coating a blend of poly(acrylic acid) and gelatin embedded with carbon black nanoparticles onto a cotton cloth, followed by salting-out and acid treatments. The acid treatment enhances the specific surface area for uranyl ion accessibility. During the SIE process, the evaporation-driven water transport can break the diffusion-limited barrier and the temperature can also be increased due to the solar-thermal effect, facilitating endothermic uranium adsorption. As a result, the hydrogel-based solar evaporator showed a significant uranium adsorption capacity of $443.2 \pm 18.1$ mg $g^{-1}$ and a water evaporation rate of 3.75 kg $m^{-2}$ when processing water spiked with 20 ppm uranium.[132]

To achieve all-weather desalination and concurrent extraction of cesium ion ($Cs^+$) from salt-lake water, Wang *et al.* designed an interfacial evaporator integrated with crown-ether-functionalized phase-change microcapsules (Crown-MicPCM). The solar-thermal conversion capability of the evaporator is derived from a polydopamine inner coating that absorbs sunlight, while the crown ether outer layer selectively adsorbs $Cs^+$. The Crown-MicPCM microcapsules use an *n*-docosane core for solar-thermal energy storage and have a magnetic $SiO_2/Fe_3O_4$ composite shell to enhance recyclability (Fig. 12e). The use of phase-change materials helps mitigate reductions in evaporation performance caused by fluctuations in solar irradiation intensity, which can vary with changing weather conditions and throughout the day. The high selectivity for $Cs^+$ extraction is due to the strong binding affinity of 18-Crown-6 and the small diameters of hydrated $Cs^+$, which closely match the cavity diameter (2.6–3.2 Å) of 18-Crown-6 (Fig. 12f). The designed evaporator demonstrated a significant $Cs^+$ adsorption capacity of 32.6 mg $g^{-1}$ and an evaporation rate of 1.43 kg $m^{-2}$ $h^{-1}$ under one-sun illumination. This performance significantly surpasses that of an evaporator without phase-change material, increasing clean water yield by 47% and improving $Cs^+$ adsorption efficiency by 12% under natural sunlight.[105]

**4.1.2 Inorganic adsorbents.** Despite significant benefits, the practical application and industrial use of organic absorbents are still limited by their low ion adsorption and high manufacturing costs. In contrast, recent years have seen a growing research interest in inorganic adsorbents. These materials are favoured due to their unique ion exchange properties, affordable price, high surface area, tunable pore structure, ease of preparation, and high stability.[133,134]

A felt woven from polypropylene/polyethylene core-sheath fibers integrated with $Li_{1.6}Mn_{1.6}O_4$ particles (DFE) has been developed (Fig. 13a).[135] The $Li_{1.6}Mn_{1.6}O_4$ particles enhance the $Li^+$ adsorption rate and capacity of the felt, utilizing solar energy to aid the process. Additionally, the hydrophilicity of the fibers facilitates the spontaneous upward transport of water and ions, preventing concentration polarization. The density of the DEF was adjusted to be less than that of water, allowing it to float on liquid lithium sources. Furthermore, the DEF can also be recycled through acid treatment to facilitate $Li^+$ desorption (Fig. 13b). The resulting DEF evaporation system demonstrated an evaporation rate of 1.15 kg $m^{-2}$ $h^{-1}$ and its efficiency can be well retained when treating simulated seawater ($\approx$100 kg) with low $Li^+$ concentration outdoors under natural sunlight (Fig. 13c). Compared to metal oxides, hydrous titania has shown better adsorption capabilities. Zhang *et al.* developed a novel separated solar evaporator consisting of a tilted n-shaped $H_2TiO_3$-modified super hydrophilic fabric and a solar-thermal sheet.[7] This design utilizes the hydrophilic fabric to transport brine to the solar-thermal sheet while providing ample sites for $Li^+$ adsorption. When the evaporator is positioned between two brine tanks, it draws brine from an elevated tank to the lower surface of the solar-thermal sheet. This setup enables SIE on the solar-thermal sheet, which also creates numerous adsorption sites for $Li^+$ selective adsorption within the water transport channels. The excess and concentrated brine is then moved to the lower tank on the opposite side, driven by capillary forces and gravity. Meanwhile, the heat from the solar-thermal sheets enhances both the kinetics and thermodynamics of $Li^+$ adsorption and aids in the evaporation process by rapidly transferring heat to the fabric. Consequently, $Li^+$ ions are captured by the $H_2TiO_3$ on the fabric and water condenses into clean water in an intermediate tank (Fig. 13d). This evaporator demonstrated excellent salt resistance and impressive water evaporation rates, achieving 1.51 kg $m^{-2}$ $h^{-1}$ with a 20 wt% brine solution.

 

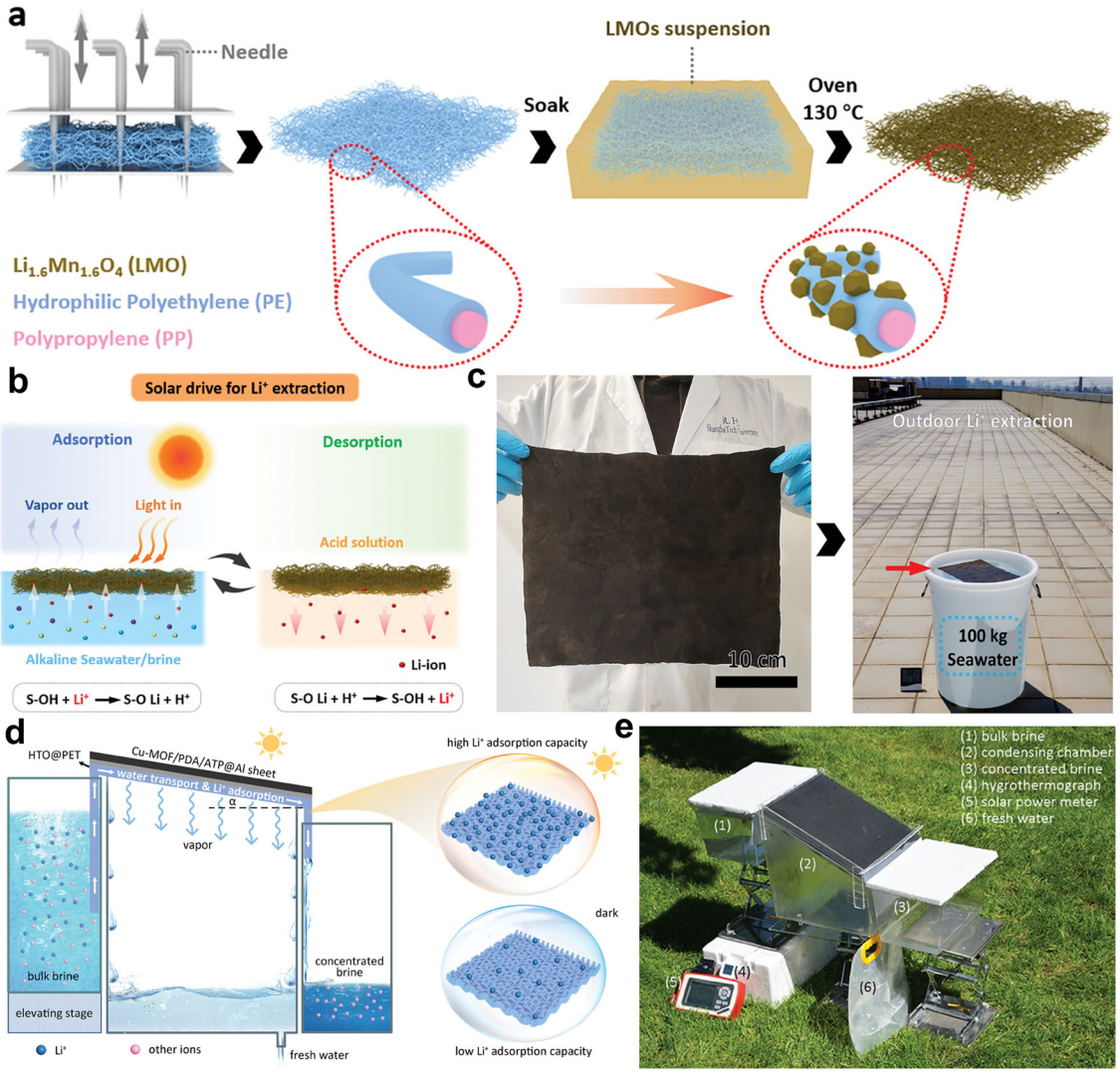


Fig. 13 (a) The schematic diagram for preparing the DEF. (b) After adsorption, the DEF was soaked in an acidic solution to obtain the $Li^+$-rich solution. (c) Digital photos of large-area DEF and its outdoor lithium extraction. Reproduced from ref. 135 with permission from copyright (2024) John Wiley & Sons. (d) Schematic illustration of simultaneous clean water collection and $Li^+$ selective adsorption using the fabric evaporator. (e) Image of the large integral prototype for simultaneous water collection and $Li^+$ adsorption. Reproduced from ref. 7 with permission from copyright (2024) John Wiley & Sons.

It also exhibited a high $Li^+$ adsorption capacity of 20.09 mg $g^{-1}$ (Fig. 13e).

### 4.2 Separation by solution and mobility variation

In addition to using adsorbent materials in the evaporator for ion capture, exploiting differences in ion solubility and mobility to separate and extract them is also effective. Ion mobility describes the rate at which ions migrate under an applied external field, with ions exhibiting higher mobility generally being more readily extracted. Conversely, solubility governs the distribution of ions in aqueous environments, with more soluble species achieving higher concentrations and thus facilitating their extraction. In practical applications, selective materials can be engineered to exploit the differential mobility and solubility of ions, enabling their effective separation and enrichment. This strategy not only enhances ion extraction efficiency but also promotes resource recovery, thereby advancing environmental remediation and resource recycling efforts. For example, Ren *et al.* developed a self-concentrating crystallization method using a twisted, slender 3D porous cellulose fiber structure.[14] The fabricated crystallizer displays unique porosity, tortuosity and hydrophilicity, which facilitate the selective extraction and spatial separation of lithium from other ions by leveraging the high solubility and mobility of lithium salts. When the crystallizer is placed in saline water and exposed to light, its porous structure can lift water up to approximately 0.6 meters through capillary action, promoting rapid evaporation from the side surface. As the evaporation continues, salts with higher concentrations and lower solubilities, such as NaCl, would crystallize at lower elevations within the crystallizer. Conversely, salts like LiCl, which have lower concentrations and higher solubilities, would migrate upward

and precipitate near the top. Consequently, different salts will reach their saturation points at varied heights, allowing sequential precipitation of salts along the crystallizer and enabling efficient spatial separation for recovery. In addition, benefiting from rapid water transport capability and high selectivity, this 3D crystallizer exhibits excellent salt collection capability and achieves high evaporation rates of 9.8 kg $m^{-2}$ $h^{-1}$.

### 4.3 Membrane separation

Ion extraction from water based on membrane separation involves utilizing the differences in ionic radii to separate ions selectively. Ions of different sizes interact with materials or surfaces in distinct ways, which can be exploited to facilitate their extraction. Smaller ions typically have higher mobility and can be more easily extracted from solutions, while larger ions may form stronger complexes with certain materials, affecting their extraction efficiency. By tailoring the design of extraction materials to the specific ionic radius, selective separation and enrichment of target ions can be achieved, contributing to more efficient resource recovery and water treatment processes. Drawing inspiration from the selective ion uptake and salt secretion mechanisms of mangroves, Jin *et al.* developed an SIE system to directly extract lithium from salt-lake brines *via* the synergistic effect of an ion separation membrane and a solar-driven evaporator (Fig. 14a).[58] The system is composed of three layers: an upper solar-thermal layer for solar energy harvesting and water evaporation, a hydrophilic porous membrane in the middle that generates capillary pressure to drive water transport and an ultrathin ion separation membrane at the bottom that permits the passage of $Li^+$ while blocking other multivalent ions (Fig. 14b). Thus, as water evaporates, solid LiCl powders can be collected directly on the surface of the evaporator. This setup achieved a high evaporation rate of 3.13 kg $m^{-2}$ $h^{-1}$. When processing artificial salt-lake brine with a high salt concentration of 348.4 g $L^{-1}$, it can significantly reduce the $Mg^{2+}/Li^+$ ratio from 19.8 to 0.3. In addition to efficient lithium extraction, effective storage for immediate use also requires further investigation. Zhu *et al.* explored solar transpiration-powered lithium extraction and storage devices that utilize natural sunlight to extract and store lithium from brine sources. The device consists of anodic aluminum oxide decorated with aluminum nanoparticles, which serve as a solar evaporator to generate a pressure gradient. This pressure gradient facilitates the extraction of lithium from the brine. Meanwhile, the extracted lithium is stored in a ceramic frit vascular storage layer (Fig. 14c).[59] The extraction of lithium can be improved by incorporating multi-stage systems. When treating a mixture of LiCl and $MgCl_2$ with a salinity of 1.0 g $L^{-1}$ and a $Mg^{2+}/Li^+$ ratio of 422, the evaporator can reduce the $Mg^{2+}/Li^+$ ratio to 2.5, which is about two orders of magnitude lower than that of a single-stage system (Fig. 14d). Finally, Fig. 15 presents a comparative evaluation of high-value ion collection strategies employed in the SIE process.

## 5 Conclusions and perspectives

Energy, the environment and water are fundamental to society, driving intensive global researches into advanced and sustainable technologies. SIE technology, which aligns with green and sustainable development principles, has been increasingly recognized for its great potential for practical applications, especially in remote areas. Recent advancements have led to the development of numerous solar evaporators, achieving significant enhancements in energy efficiency and clean water production capability. Moreover, these evaporators can be engineered to perform multiple functions during clean water

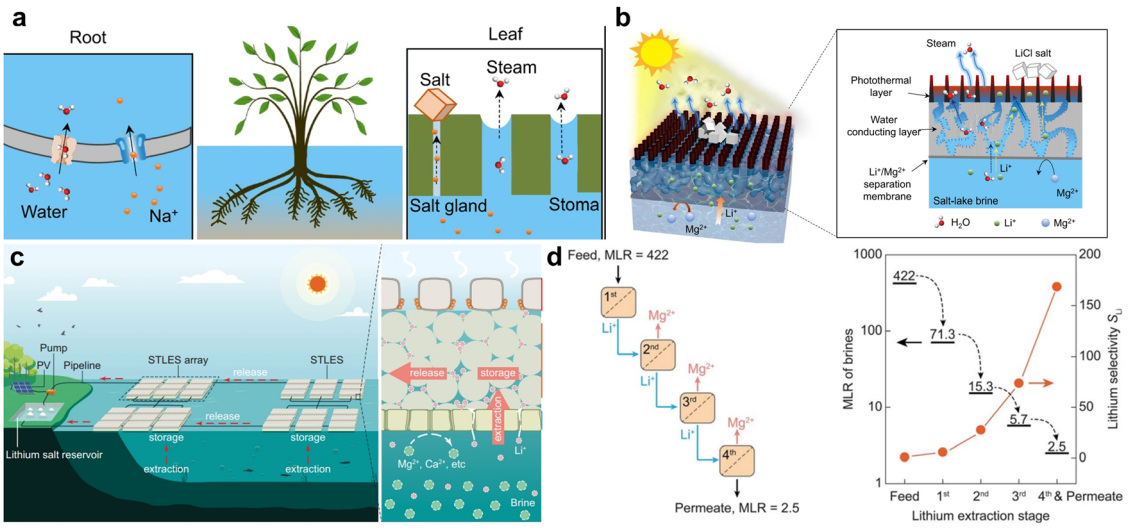


Fig. 14 (a) A schematic of regulating water and ion intake and release in mangroves. (b) Working principle of polyamide membrane-based solar-driven lithium extraction. Reproduced from ref. 58 with permission from copyright (2024) Springer Nature. (c) As prepared system can float and extract lithium from brines at scale using only ambient sunlight as the energy source–PV, photovoltaic array. (d) Schematic of staged extraction and the corresponding lithium selectivity as a function of the number of lithium extraction stages. Reproduced from ref. 59 with permission from copyright (2024) Springer Nature.

 

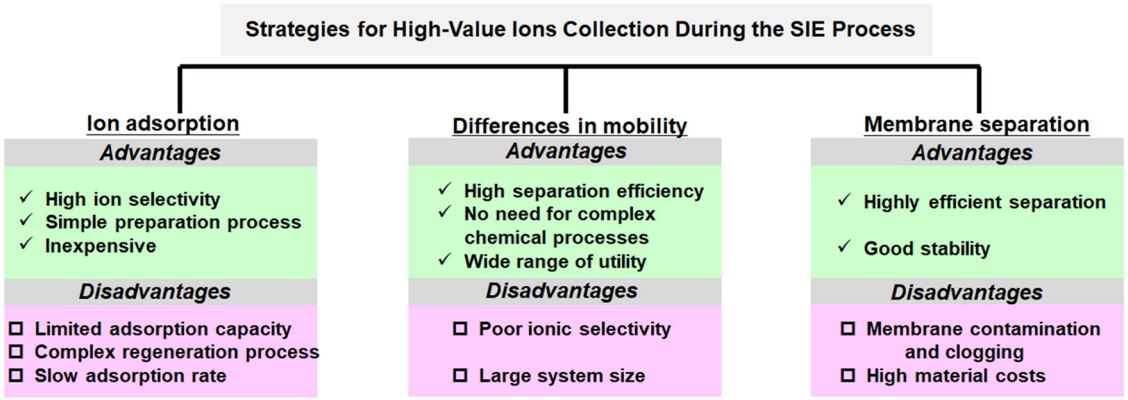


Fig. 15 Comparison of the strategies for high-value ion collection during the SIE process.

production, including pollutant removal, electrical energy generation and high-value mineral ion extraction, thus enabling more effective solar energy utilization. However, significant challenges remain that must be addressed to advance this technology further. Typically, the multiscale structural designs, material compositions, geometrical characteristics and component configurations of these SIE systems are crucial for achieving multifunctionality and enhancing overall performance. The features and their relationships with the ultimate properties of the resulting SIE system should be thoroughly investigated and revealed. This is essential for further boosting the performance, applicability and custom design of next-generation SIE systems. In particular, while many multifunctional solar evaporators have been developed for laboratory demonstration, scaling them up for large-scale production and application remains challenging due to limitations in preparation methods. The mechanical robustness, durability and application versatility of SIE systems, which have often been overlooked in prior studies, remain critical concerns, especially given the complex and variable nature of the external environment. Further researches are necessary to address these challenges effectively.

The design of multifunctional SIE systems has been proven a viable solution for achieving simultaneous clean water production and high-value ion extraction. However, the dynamics of energy transfer and conversion within these multifunctional SIE systems remain poorly understood. Gaining deeper insights into the energy flow of the system could lead to optimized thermal management, enhanced energy efficiency, increased evaporation rates and more informed designs for potential applications. In addition, while both evaporation and ion harvesting are energy-absorbing processes, the intricacies of their interrelationship have yet to be fully elucidated. Further exploration and understanding of these aspects are crucial to facilitate synergistic enhancements in performance, thereby making these systems more efficient.

In addition to performance requirements, the design of collection components within the SIE systems must also adhere to specific criteria optimized for effective outdoor operation. Typically, during use, a SIE device is enclosed and topped with a transparent polymer or glass cover to allow sunlight entry and facilitate vapor condensation. As vapor condenses, it releases latent heat onto the inner surface of the cover, resulting in the formation of water droplets. However, these water droplets can cause significant optical losses of up to 35%, thereby hindering the full utilization of solar energy and reducing the overall solar-to-vapor efficiency of the system. Moreover, the condensate formed on the cover would act as a thermal barrier that further impedes the condensation process. As a result, the overall efficiency of converting solar energy to collected water is limited. This efficiency is considerably lower than the ultra-high efficiency (90%) achieved in open systems.[52] Furthermore, the high humidity within the enclosure can also interfere with the salt crystallization process, thus affecting the mineral ion extraction performance.

The integration of functional adsorbent materials into the SIE system is the most straightforward approach to optimizing ion extraction capability. Achieving a uniform distribution of these adsorbent materials within the SIE device is crucial for effective ion adsorption on a large scale. A major challenge is establishing strong interactions between the adsorbent materials and the evaporation system, which is essential for ensuring the long-term stability of the devices. Another significant challenge is the time lag between the solar evaporation and ion collection processes, which hinders the enhancement of the ion collection rate. The efficiency of ion extraction is affected by the concentration of the ions in the source water and their ratio to impurity ions. When ion concentrations and occupancy ratios are low, extraction efficiency decreases, making it challenging to complete the extraction within the designated evaporation time. Therefore, there is a pressing need to develop innovative material designs and efficient extraction techniques that can be integrated into the multifunctional SIE systems to enable rapid and highly selective ion extraction at low concentrations. In addition, current research primarily focuses on extracting specific ions (*e.g.* $Na^+$, $Li^+$, $U^+$ and $CS^+$) during seawater desalination. However, seawater contains a variety of complex and valuable ions, requiring methods that can simultaneously and precisely separate these ions to optimize resource utilization efficiently.

The integration of SIE with the high-value ion extraction process has demonstrated significant promise in advancing

next-generation water-energy technologies. Further enhancing the performance of multifunctional SIE devices requires the combination of computational modeling-assisted design and precise structural control and tuning techniques. This approach is crucial for achieving a more accurate and detailed mechanistic understanding of these devices, thereby boosting their performance. The use of advanced characterization tools will also help reveal the underlying mechanisms. Additionally, incorporating additional functionalities such as catalysis, sterilization, and electricity generation into multi-functional SIE systems can maximize the efficient use of solar energy. These innovations are also expected to address the stringent demands of effective clean water collection and resource extraction in next-generation applications. Ultimately, the development of advanced multifunctional SIE systems that harness inexhaustible solar energy holds the promise of alleviating the global clean water crisis and contributing significantly to rapid economic and societal development.

## Data availability

No primary research results, software or code have been included and no new data were generated or analysed as part of this review.

## Conflicts of interest

There are no conflicts to declare.

## Acknowledgements

This research is supported by the National Natural Science Foundation of China (U23A20587, 52221006, 52090034, U22A20248).

## References

1 J. J. Urban, *Joule*, 2017, **1**, 665.
2 G. Ni, S. H. Zandavi, S. M. Javid, S. V. Boriskina, T. A. Cooper and G. Chen, *Energy Environ. Sci.*, 2018, **11**, 1510.
3 M. T. Ali, H. E. S. Fath and P. R. Armstrong, *Renewable Sustainable Energy Rev.*, 2021, **15**, 4187.
4 C. Li, Y. Goswami and E. Stefanakos, *Renewable Sustainable Energy Rev.*, 2013, **19**, 136.
5 Z. Wang, X. Wu, F. He, S. Peng and Y. Li, *Adv. Funct. Mater.*, 2021, **31**, 2011114.
6 H. Sun, Y. Li, J. Li, Z. Zhu, W. Zhang, W. Liang, C. Ma and A. Li, *ACS Appl. Mater. Interfaces*, 2021, **13**, 33427.
7 K. Chen, L. Li, B. Li, Y. Yang, K. Zhu and J. Zhang, *Adv. Funct. Mater.*, 2024, **34**, 2402221.
8 A. Kondori, M. Esmaeilirad, A. M. Harzandi, R. Amine, M. T. Saray, L. Yu, T. Liu, J. Wen, N. Shan, H.-H. Wang, A. T. Ngo, P. C. Redfern, C. S. Johnson, K. Amine, R. S. Yassar, L. A. Curtiss and M. Asadi, *Science*, 2023, **379**, 499.
9 S. Chen, Z. Nie, F. Tian, L. Nie, R. Wei, J. Yu, T. Gao, Z. Sun, N. Yang and W. Liu, *Adv. Funct. Mater.*, 2022, **32**, 2113318.
10 C. Zhang, X. Hu, Z. Nie, C. Wu, N. Zheng, S. Chen, Y. Yang, R. Wei, J. Yu, N. Yang, Y. Yu and W. Liu, *J. Adv. Ceram.*, 2022, **11**, 1530.
11 Y. Guo, X. Zhang, S. Jin, Q. Xia, Y. Chang, L. Wang and A. Zhou, *J. Adv. Ceram.*, 2023, **12**, 1889.
12 M. Keener, C. Hunt, T. G. Carroll, V. Kampel, R. Dobrovetsky, T. W. Hayton and G. Ménard, *Nature*, 2020, **577**, 652.
13 S. Yang, F. Zhang, H. Ding, P. He and H. Zhou, *Joule*, 2018, **2**, 1648.
14 X. Chen, M. Yang, S. Zheng, F. T. Coleto, Q. Dong, G. Cheng, N. Yao, H. A. Stone, L. Hu and Z. J. Ren, *Nat. Water*, 2023, **1**, 808.
15 Z. Li, I. C. Chen, L. Cao, X. Liu, K. W. Huang and Z. Lai, *Science*, 2024, **385**, 1438.
16 H. Wang, T. Xu, B. Zheng, M. Cao, F. Gao, G. Zhou, C. Ma, J. Dang, W. Yao, K. Wu, T. Liu, Y. Yuan, Q. Fu and N. Wang, *J. Hazard. Mater.*, 2022, **433**, 128789.
17 N. Li, J. Wu, R. Su, N. Zhang, J. Zhao and Z. Wang, *Desalination*, 2023, **545**, 116153.
18 C. W. Abney, R. T. Mayes, T. Saito and S. Dai, *Chem. Rev.*, 2017, **117**, 13935.
19 C. Wang, J. Wang, Z. Li, K. Xu, T. Lei and W. Weike, *J. Mater. Chem. A*, 2020, **8**, 9528.
20 J. Hou, H. Zhang, A. W. Thornton, A. J. Hill, H. Wang and K. Konstas, *Adv. Funct. Mater.*, 2021, **31**, 2105991.
21 B. K. Pramanik, L. Shu and V. Jegatheesan, *J. Environ. Sci. Water Resour.*, 2017, **3**, 625.
22 A. F. Razi, A. Pendashteh, L. C. Abdullah, D. R. A. Biak, S. S. Madaeni and Z. Z. Abidin, *J. Hazard. Mater.*, 2009, **170**, 530.
23 C. J. Gabelich, A. Rahardianto, C. R. Northrup, T. I. Yun and Y. Cohen, *Desalination*, 2011, **272**, 36.
24 J. Morillo, J. Usero, D. Rosado, H. E. Bakouri, A. Riaza and F.-J. Bernaola, *Desalination*, 2014, **336**, 32.
25 T. Tong and M. Elimelech, *Environ. Sci. Technol.*, 2016, **50**, 6846.
26 D. Xevgenos, K. Moustakas, D. Malamis and M. Loizidou, *Desalin. Water Treat.*, 2016, **57**, 2304.
27 W. R. Cui, F. F. Li, R. H. Xu, C. R. Zhang, X. R. Chen, R. H. Yan, R. P. Liang and J. D. Qiu, *Angew. Chem., Int. Ed.*, 2020, **59**, 17684.
28 Y. Yuan, B. Niu, Q. Yu, X. Guo, Z. Guo, J. Wen, T. Liu, H. Zhang and N. Wang, *Angew. Chem., Int. Ed.*, 2019, **59**, 1220.
29 H.-N. Li, C. Zhang, J.-H. Xin, Y.-W. Liu, H.-C. Yang, C.-Y. Zhu, C. Liu and Z.-K. Xu, *ACS Nano*, 2024, **18**, 2434.
30 L. Zhu, M. Gao, C. K. N. Peh and G. W. Ho, *Mater. Horiz.*, 2018, **5**, 323.
31 S. Karami, F. A. Roghabadi, M. Maleki, V. Ahmadi and S. M. Sadrameli, *Sol. Energy*, 2021, **225**, 747.
32 P. Zhang, Q. Liao, H. Yao, Y. Huang, H. Cheng and L. Qu, *Energy Storage Mater.*, 2019, **18**, 429.

 

33 F. Zhao, Y. Guo, X. Zhou, W. Shi and G. Yu, *Nat. Rev. Mater.*, 2020, **5**, 388.
34 V.-D. Dao, N. H. Vu and S. Yun, *Nano Energy*, 2020, **68**, 104324.
35 X. Liu, D. D. Mishra, X. Wang, H. Peng and C. Hu, *J. Mater. Chem. A*, 2020, **8**, 17907.
36 T.-S. D. Le, D. Yang, H. K. Nam, Y. Lee, C. T. Lim, B. J. Lee, S.-W. K and Y.-J. Kim, *ACS Nano*, 2024, **18**, 33220.
37 B. Xu, M. Ganesan, R. K. Devi, X. Ruan, W. Chen, C. C. Lin, H. T. Chang, E. Lizundia, A. K. An and S. K. Ravi, *Adv. Mater.*, 2024, **37**, 2406666.
38 Z. W. Seh, S. Liu, M. Low, S.-Y. Zhang, Z. Liu, A. Mlayah and M.-Y. Han, *Adv. Mater.*, 2012, **24**, 2310.
39 R. Long, Y. Li, L. Song and Y. Xiong, *Small*, 2015, **11**, 3873.
40 M. L. Brongersma, N. J. Halas and P. Nordlander, *Nat. Nanotechnol.*, 2015, **10**, 25.
41 D. J. Aberasturi, A. B. Serrano-Montes and L. M. Liz-Marzán, *Adv. Opt. Mater.*, 2015, **3**, 602.
42 J. A. Webb and R. Bardhan, *Nanoscale*, 2014, **6**, 2502.
43 A. Lalisse, G. Tessier, J. Plain and G. Baffou, *J. Phys. Chem. C*, 2015, **119**, 25518.
44 J. S. Biggins, S. Yazdi and E. Ringe, *Nano Lett.*, 2018, **18**, 3752.
45 C. Langhammer, M. Schwind, B. Kasemo and I. Zoric, *Nano Lett.*, 2018, **8**, 1461.
46 P. Zheng, H. Tang, B. Liu, S. Kasani, L. Huang and N. Wu, *Nano Res.*, 2019, **12**, 63.
47 H. Y. Lee, M. S. Kwak, G. T. Hwang, H. S. Ahn, D. H. Ha and S. N. Yi, *Appl. Surf. Sci.*, 2022, **596**, 153588.
48 I. Pastoriza-Santos and L. M. Liz-Marzán, *Adv. Funct. Mater.*, 2009, **19**, 679.
49 C. Xu, Q. Tang, W. Tu and L. Wang, *Energy Environ. Sci.*, 2024, **17**, 4461.
50 Q. Tian, M. Tang, Y. Sun, R. Zou, Z. Chen, M. Zhu, S. Yan, J. Wang, J. Wang and J. Hu, *Adv. Mater.*, 2011, **23**, 3542.
51 C. M. Hessel, V. P. Pattani, M. Rasch, M. G. Panthani, B. Koo, J. W. Tunnell and B. A. Korgel, *Nano Lett.*, 2011, **11**, 2560.
52 M. Gao, L. Zhu, C. K. Peh and G. W. Ho, *Energy Environ. Sci.*, 2019, **12**, 841.
53 G. Zhang, C. Hai, Y. Zhou, W. Tang, J. Zhang, J. Zeng, Y. Liu, S. Dong and G. Peng, *Chem. Eng. J.*, 2022, **450**, 137912.
54 X. Chen, C. Wu, Y. Lv, C. Zhang, X. Zhang, L. Nie, Y. Zhang, L. Zhao, C. Huang and W. Liu, *Matter*, 2022, **5**, 3053.
55 S. Yuan, L. Huang, Z. Huang, D. Sun, J. S. Qin, L. Feng, J. Li, X. Zou, T. Cagin and H. C. Zhou, *J. Am. Chem. Soc.*, 2020, **142**, 4732.
56 Y. Guo, Y. Ying, Y. Mao, X. Peng and B. Chen, *Angew. Chem., Int. Ed.*, 2016, **55**, 15120.
57 H. Q. Liang, Y. Guo, X. Peng and B. Chen, *J. Mater. Chem. A*, 2020, **8**, 11399.
58 S. Zhang, X. Wei, X. Cao, M. Peng, M. Wang, L. Jiang and J. Jin, *Nat. Commun.*, 2024, **15**, 238.
59 Y. Song, S. Fang, N. Xu, M. Wang, S. Chen, J. Chen, B. Mi and J. Zhu, *Science*, 2024, **385**, 1444.
60 Y. Oren, E. Korngold, N. Daltrophe, R. Messalem, Y. Volkman, L. Aronov, M. Weismann, N. Bouriakov, P. Glueckstern and J. Gilron, *Desalination*, 2010, **261**, 321.
61 C. Dang, H. Wang, Y. Cao, J. Shen, J. Zhang, L. Lv, G. Xu and M. Zhu, *Energy Environ. Sci.*, 2022, **15**, 5405.
62 S. Wang, Y. Niu, L. Yan, Y. Jing, Z. Zhu, H. Sun, J. Li, W. Liang and A. Li, *J. Environ. Chem. Eng.*, 2022, **10**, 108254.
63 L. Li and J. Zhang, *Nano Energy*, 2021, **81**, 105682.
64 Y. Xia, Y. Li, S. Yuan, Y. Kang, M. Jian, Q. Hou, L. Gao, H. Wang and X. Zhang, *J. Mater. Chem. A*, 2020, **8**, 16212.
65 W. Xu, X. Hu, S. Zhuang, Y. Wang, X. Li, L. Zhou, S. Zhu and J. Zhu, *Adv. Energy Mater.*, 2018, **8**, 1702884.
66 S. He, C. Chen, Y. Kuang, R. Mi, Y. Liu, Y. Pei, W. Kong, W. Gan, H. Xie, E. Hitz, C. Jia, X. Chen, A. Gong, J. Liao, J. Li, Z. J. Ren, B. Yang, S. Das and L. Hu, *Energy Environ. Sci.*, 2019, **12**, 1558.
67 Y.-Q. Luo, F. Song, J.-M. Wu, F. Wang, X.-L. Wang and Y.-Z. Wang, *Chem. Eng. J.*, 2021, **421**, 129824.
68 X. Zhou, F. Zhao, Y. Guo, Y. Zhang and G. Yu, *Energy Environ. Sci.*, 2018, **11**, 1985.
69 K. Elsaid, M. Kamil, E. T. Sayed, M. A. Abdelkareem, T. Wilberforce and A. Olabi, *Sci. Total Environ.*, 2020, **748**, 141528.
70 A. Panagopoulos, K.-J. Haralambous and M. Loizidou, *Sci. Total Environ.*, 2019, **693**, 133545.
71 C. Finnerty, L. Zhang, D. L. Sedlak, K. L. Nelson and B. Mi, *Environ. Sci. Technol.*, 2017, **51**, 11701.
72 C. Zhang, Y. Shi, L. Shi, H. Li, R. Li, S. Hong, S. Zhuo, T. Zhang and P. Wang, *Nat. Commun.*, 2021, **12**, 998.
73 Z. Wang, J. Gao, J. Zhou, J. Gong, L. Shang, H. Ye, F. He, S. Peng, Z. Lin, Y. Li and F. Caruso, *Adv. Mater.*, 2022, **35**, 2209015.
74 L. Wu, Z. Dong, Z. Cai, T. Ganapathy, N. X. Fang, C. Li, C. Yu, Y. Zhang and Y. Song, *Nat. Commun.*, 2020, **11**, 521.
75 Y. Xia, Q. Hou, H. Jubaer, Y. Li, Y. Kang, S. Yuan, H. Liu, M. W. Woo, L. Zhang, L. Gao, H. Wang and X. Zhang, *Energy Environ. Sci.*, 2019, **12**, 1840.
76 R. Gu, Z. Yu, Y. Sun, P. Xie, Y. Li and S. Cheng, *Desalination*, 2022, **524**, 115470.
77 Z. Yu, S. Li, Y. Chen, X. Zhang, J. Chu, Y. Zhang and S. C. Tan, *Desalination*, 2022, **539**, 115942.
78 Z. Lei, X. Sun, S. Zhu, K. Dong, X. Liu, L. Wang, X. Zhang, L. Qu and X. Zhang, *Nano-Micro Lett.*, 2022, **14**, 10.
79 G. W. K. Moore, S. E. L. Howell, M. Brady, X. Xu and K. McNeil, *Nat. Commun.*, 2021, **12**, 1.
80 Y. Shi, C. Zhang, R. Li, S. Zhuo, Y. Jin, L. Shi, S. Hong, J. Chang, C. Ong and P. Wang, *Environ. Sci. Technol.*, 2018, **52**, 11822.
81 M. Ding, H. Lu, Y. Sun, Y. He, J. Yu, H. Kong, C. Shao, C. Y. Liu and C. Li, *Adv. Sci.*, 2022, **9**, 2205202.
82 H. Liu, R. Jin, S. Duan, Y. Ju, Z. Wang, K. Yang, B. Wang, B. Wang, Y. Yao and F. Chen, *Small*, 2021, **17**, 2100969.
83 H. Zhao, X. Li and X. Du, *Mater. Today Sustain.*, 2023, **24**, 100538.
84 X. Wang, Q. Gan, R. Chen, H. Peng, T. Zhang and M. Ye, *ACS Sustainable Chem. Eng.*, 2020, **8**, 7753.

85 Y. Shao, J. Tang, N. Li, T. Sun, L. Yang, D. Chen, H. Zhi, D. Wang, H. Liu and G. Xue, *EcoMat*, 2020, **2**, 1.
86 R. Gu, Z. Yu, Y. Sun, Y. Su, W. Wu and S. Cheng, *Desalination*, 2022, **537**, 115862.
87 M. Ding, D. Zhao, P. Feng, B. Wang, Z. Duan, R. Wei, Y. Zhao, C. Y. Liu and C. Li, *Carbon Energy*, 2024, **6**, e548.
88 X. Dong, H. Li, L. Gao, C. Chen, X. Shi, Y. Du and H. Deng, *Small*, 2022, **18**, 2107156.
89 L. Li, N. He, B. Jiang, K. Yu, Q. Zhang, H. Zhang, D. Tang and Y. Song, *Adv. Funct. Mater.*, 2021, **31**, 2104380.
90 M. A. Abdelsalam, M. Sajjad, A. Raza, F. AlMarzooqi and T. Zhang, *Nat. Commun.*, 2024, **15**, 874.
91 S. Sun, C. Shi, Y. Kuang, M. Li, S. Li, H. Chan, S. Zhang, G. Chen, A. Nilghaz, R. Cao and J. Tian, *Water Res.*, 2022, **226**, 119279.
92 T.-S. Wong, S. H. Kang, S. K. Y. Tang, E. J. Smythe, B. D. Hatton, A. Grinthal and J. Aizenberg, *Nature*, 2011, **477**, 443.
93 X. Yao, S. Wu, L. Chen, J. Ju, Z. Gu, M. Liu, J. Wang and L. Jiang, *Angew. Chem., Int. Ed.*, 2015, **54**, 8975.
94 P. Kim, T.-S. Wong, J. Alvarenga, M. J. Kreder, W. E. Adorno-Martinez and J. Aizenberg, *ACS Nano*, 2012, **8**, 6569.
95 K. Rykaczewski, S. Anand, S. B. Subramanyam and K. K. Varanasi, *Langmuir*, 2013, **29**, 5230.
96 W. S. Y. Wong, K. I. Hegner, V. Donadei, L. Hauer, A. Naga and D. Vollmer, *Nano Lett.*, 2020, **20**, 8508.
97 Y. Q. Luo, X. Yao, L. Zhao, L. Liu, Y. Zhou, L. Jiang and J. Ju, *Adv. Funct. Mater.*, 2023, **33**, 2301086.
98 A. Dhyani, J. Wang, A. K. Halvey, B. Macdonald, G. Mehta and A. Tuteja, *Science*, 2021, **373**, 294.
99 D. Mampallil and H. B. Eral, *Adv. Colloid Interface Sci.*, 2018, **252**, 38.
100 H. Peng, D. Wang and S. Fu, *ACS Appl. Mater. Interfaces*, 2021, **13**, 47549.
101 Y. Bian, Z. Ye, G. Zhao, K. Tang, Y. Teng, S. Chen, L. Zhao, X. Yuan, S. Zhu, J. Ye, H. Lu, Y. Yang, L. Fu and S. Gu, *ACS Appl. Mater. Interfaces*, 2022, **14**, 34151.
102 Y. Wang, X. Wu, P. Wu, H. Yu, J. Zhao, X. Yang, Q. Li, Z. Zhang, D. Zhang, G. Owens and H. Xu, *J. Mater. Chem. A*, 2022, **10**, 14470.
103 T. A. Cooper, S. H. Zandavi, G. W. Ni, Y. Tsurimaki, Y. Huang, S. V. Boriskina and G. Chen, *Nat. Commun.*, 2018, **9**, 5086.
104 L. Wang, Z. Liu, J. Xu, K. Wang, Q. Wang and G. Liu, *Desalination*, 2023, **567**, 116993.
105 H. Zhang, S. Zhou, H. Liu, Z. Qian and X. Wang, *Adv. Funct. Mater.*, 2024, **34**, 2408269.
106 P. Wu, X. Wu, Y. Wang, J. Zhao, H. Xu and G. Owens, *Green Energy Environ.*, 2023, **8**, 1459.
107 X. Sun, Z. Liu, F. Zhao and H. Hao, *Environ. Sci. Technol.*, 2021, **55**, 12180.
108 P. Greim, A. A. Solomon and C. Breyer, *Nat. Commun.*, 2020, **11**, 4570.
109 A. Goldthau and L. Hughes, *Nature*, 2020, **585**, 28.
110 M. Wang, T. Zhang, Z. Meng, C. Wang, W. Dong, J. Liu, S. Yang, X. Hou, X. Cheng, W. Liu, C. Xing, X. Liu and J. Zhou, *Chem. Eng. J.*, 2023, **458**, 141403.
111 L. Tang, S. Huang, Y. Wang, D. Liang, Y. Li, J. Li, Y. Wang, Y. Xie and W. Wang, *ACS Appl. Mater. Interfaces*, 2020, **12**, 9775.
112 S. Wei, Y. Wei, T. Chen, C. Liu and Y. Tang, *Chem. Eng. J.*, 2020, **379**, 122407.
113 P. Tao, G. Ni, C. Song, W. Shang, J. Wu, J. Zhu, G. Chen and T. Deng, *Nat. Energy*, 2018, **3**, 1031.
114 N. Xu, J. Li, C. Finnerty, Y. Song, L. Zhou, B. Zhu, P. Wang, B. Mi and J. Zhu, *Nat. Water*, 2023, **1**, 494.
115 C. Chen, Y. Kuang and L. Hu, *Joule*, 2019, **3**, 683.
116 L. Zhou, X. Li, G. W. Ni, S. Zhu and J. Zhu, *Natl. Sci. Rev.*, 2019, **6**, 562.
117 L. Zhang, Z. Xu, L. Zhao, B. Bhatia, Y. Zhong, S. Gong and E. N. Wang, *Energy Environ. Sci.*, 2021, **14**, 1771.
118 T. Ding, Y. Zhou, W. L. Ong and G. W. Ho, *Mater. Today*, 2021, **42**, 178.
119 A. Razmjou, M. Asadnia, E. Hosseini, A. H. Korayem and V. Chen, *Nat. Commun.*, 2019, **10**, 5793.
120 H. Pauwels, M. Brach and C. Fouillac, *Colloids Surf., A*, 1995, **100**, 73.
121 S. Bi, P. Thiruvengadam, S. Wei, W. Zhang, F. Zhang, L. Gao, J. Xu, D. Wu, J.-S. Chen and F. Zhang, *J. Am. Chem. Soc.*, 2020, **142**, 11893.
122 W.-R. Cui, C.-R. Zhang, R.-H. Xu, X.-R. Chen, R.-H. Yan, W. Jiang, R.-P. Liang and J.-D. Qiu, *ACS EST Water*, 2020, **1**, 440.
123 W.-S. Chen, C.-H. Lee and H.-J. Ho, *Appl. Sci.*, 2018, **8**, 2252.
124 F. Arroyo, J. Morillo, J. Usero, D. Rosado and H. E. Bakouri, *Desalination*, 2019, **468**, 114073.
125 F. Wu, D. Liu, G. Li, L. Li, L. Yan, G. Hong and X. Zhang, *Nanoscale*, 2021, **13**, 5419.
126 W.-R. Cui, C.-R. Zhang, R.-P. Liang, J. Liu and J.-D. Qiu, *ACS Appl. Mater. Interfaces*, 2021, **13**, 31561.
127 W.-R. Cui, C.-R. Zhang, R.-P. Liang and J.-D. Qiu, *J. Mater. Chem. A*, 2021, **9**, 25611.
128 J. Zhou, X. Li, W. Xie, Q. Chen, Y. Jiang, X. Wu and L. Yang, *J. Cleaner Prod.*, 2024, **437**, 140523.
129 H. Liang, Y. Mu, M. Yin, P. He and W. Guo, *Sci. Adv.*, 2023, **9**, eadj1677.
130 F. Zhao, X. Zhou, Y. Shi, X. Qian, M. Alexander, X. Zhao, S. Mendez, R. Yang, L. Qu and G. Yu, *Nat. Nanotechnol.*, 2018, **13**, 489.
131 Y. Guo, F. Zhao, X. Zhou, Z. Chen and G. Yu, *Nano Lett.*, 2019, **19**, 2530.
132 Z. Liu, K. Feng, X. Zhang, L. Fu, J. Ren, R. Gao, S. Ding, W. Xing, Y. Li, J. Cheng, Q. Li, J. Gong and R. Niu, *Chem. Eng. J.*, 2024, **498**, 155423.
133 C. W. Chen, P. A. Chen, C. J. Wei, H. L. Huang, C. J. Jou, Y. L. Wei and H. P. Wang, *Mar. Pollut. Bull.*, 2017, **124**, 1106.
134 H. Park, N. Singhal and E. H. Jho, *Water Res.*, 2015, **87**, 320.
135 X. Chen, W. Yu, Y. Zhang, C. Huang, L. Nie, J. Yu, Y. Zhang, C. Zhang, W. Zhai, X. Zhang, Y. Yu and W. Liu, *Adv. Funct. Mater.*, 2024, **34**, 2316178.

 